DOI: 10.1002/ (please add manuscript number)
Article type: Full Paper

Spectrally-Tailored Hygroscopic Hydrogels with Janus Interfaces for Hybrid Passive Cooling of Solar Cells

Shuai Li, *Suxu Wang*, *Jun Zhao*, *Zhihang Wang**, *Petri Murto*, *Liangmin Yu*, *Junwu Chen** & *Xiaofeng Xu**

S. Li, S. Wang, J. Zhao

Prof. X. Xu, email: xuxiaofeng@ouc.edu.cn

College of Materials Science and Engineering, Ocean University of China, Qingdao 266100, China.

Dr. Z. Wang, email: z.wang@derby.ac.uk

School of Engineering, College of Science and Engineering, University of Derby, Markeaton Street, Derby DE22 3AW, United Kingdom.

Department of Materials Science and Metallurgy, University of Cambridge, 27 Charles Babbage Road, Cambridge, CB3 0FS, United Kingdom.

Dr. P. Murto

Department of Chemistry and Materials Science, Aalto University, Kemistintie 1, 02150 Espoo, Finland.

Prof. L. Yu

Key Laboratory of Marine Chemistry Theory and Technology, Ministry of Education, Ocean University of China, Qingdao 266100, China.

Prof. J. Chen, email: psjwchen@scut.edu.cn

Institute of Polymer Optoelectronic Materials & Devices, State Key Laboratory of Luminescent Materials & Devices, South China University of Technology, Guangzhou 510640, China

Keywords: *hygroscopic hydrogels*, *highly entangled polymers*, *Janus membranes*, *hybrid passive cooling*, *solar power generation*

Abstract

Energy-efficient thermal management is critical for addressing the inevitable heat generation and inefficient heat dissipation of conventional solar cells. Designing cooling systems that optimize optical windows, solar conversion, interfacial properties and aesthetic appeal for diverse photovoltaic technologies remains a significant challenge. Herein, passive cooling membranes are developed as “front surfaces” for both silicon-based (inorganic) and polymer (organic) solar cells. The LiCl-embedded hydrogel combines highly cross-linked and highly entangled polymers within a two-layered membrane. The salt-in effect of highly concentrated zwitterionic copolymers and large-volume swelling of hydrogels ensure high LiCl retention (max. 20 wt%) with negligible leakage, leading to stable evaporative cooling. This membrane is also distinguished by its Janus-like surfaces and tailored optical windows, integrating high transmittance (~90%) for the sunlight absorption and high emissivity (~98%) for sky radiative cooling. Our study represents one of the few examples of integrating hybrid cooling mechanisms on solar panels, achieving a maximized efficiency increase above 21% under natural sunlight while enhancing cooling power regeneration overnight. Moreover, its cooling power and durability enable ~95% of efficiency retention over 10000 bending cycles in flexible solar cells. This study shines a light on developing hierarchically aligned hydrogels for self-contained and user-defined thermal management for diverse electronics.

1. Introduction

Solar energy, characterized by its abundance, accessibility and renewability, plays a crucial role in mitigating the global energy crisis, reducing carbon footprints and driving progress toward achieving net-zero emissions. At present, silicon-based solar cells (photovoltaic cells) dominate the global market, driving the widespread adoption of solar power as a cost-competitive and reliable energy source.[1] Meanwhile, emerging alternatives such as organic, perovskite, heterojunction and tandem solar cells offer the potential for superior performance, cost-efficient production, enhanced integration capabilities, and greater aesthetic versatility.[2-5]

Conventional single-junction solar cells typically convert 10 − 25 % of incident sunlight into electricity. However, no semiconductor can fully absorb the solar spectrum across the ultraviolet (UV) to infrared (IR) region (0.2 − 2.6 μm). Regardless of the solar cell type, photons with energies exceeding the band gap are generally lost as heat (thermalization loss), while sub-band-gap photons that are either unconverted or reflected also contribute to heat generation.[6] As a result, the thermal power per square meter can exceed 600 W in solar panels.[7] The accumulated heat results in an inevitable rise in the operating temperature of solar cells, exceeding ~50°C above the ambient temperature. Previous studies have evidenced that conventional *c*-Si solar cells experience an efficiency decline of ~0.45 % per °C increase in operating temperature.[8] Elevated temperatures also exacerbate the degradation of solar modules by accelerating failures in adhesive seals, corrosion and interconnections — issues that undermine energy yield, shorten module lifespan, and increase the levelized cost of energy for solar cells.[9] Consequently, the development of thermal interface materials and thermal management strategies are crucial for the majority of solar technologies.[10-11] Active cooling techniques, such as water spraying or forced air ventilation, have been proposed for densely packed solar arrays. However, these methods often require complex engineering solutions, consume additional energy, and may ultimately reduce the net power output of solar systems.[8]

Passive cooling is particularly suited for individual, off-grid solar panels, offering the advantage of zero energy consumption and broader applicability.[7] Traditional passive cooling strategies primarily focus on mounting configurations and installation locations of solar panels, optimizing the operating environment (i.e., low ambient temperature, high wind speed and high atmospheric transparency) to promote cooling power. A notable example is the emerging technology of floating solar cells, where the cooling effect of water bodies could improve photovoltaic performance by up to ~10% in warm climates.[12] Recent advancements in passive cooling for solar cells focus on integrating hardware-based cooling components with solar panels. These designs include combining solar cells with evaporative systems,[13-15] incorporating phase-change/energy storage materials,[16-17] or developing multi-layered films for sky radiative cooling.[18] Despite these innovations, several challenges persist, including spectral mismatch, trade-offs between maximizing solar exposure and ensuring optimal cooling capacity, potential liquid leakage and complex fabrication.[9]

Water is widely regarded as the most effective working fluid for liquid−vapor phase change and evaporative cooling, due to its high thermal conductivity, substantial enthalpy of vaporization (> 2000 J g^{-1}), and strong absorption of sunlight, especially in the near-infrared (NIR) wavelength range.[19-20] Recent advancements in micro- and nanoengineering have significantly enhanced heat transfer during vaporization processes.[21-22] Therefore, evaporative cooling systems integrated with solar cells have gained growing attention in recent years.[7] Hybrid systems that combine solar panels with tandem or multi-stage solar stills have been developed to scale up total solar energy conversion.[23-30] Notably, the water used for passive cooling can be sourced not only from liquid water but also from atmospheric water vapor, which is naturally replenished through the hydrological cycle, ensuring a sustainable supply. Sorption-based energy generation represents a promising strategy for obtaining heat, cold and electricity from ubiquitous moisture.[31] In particular, recent development of hygroscopic salt-embedded

composites (i.e., fabrics, aerogels, hydrogels and foams) with multiscale hierarchical structures has demonstrated for high sorption/desorption capacities, rapid kinetics, flexible integration and system-level design across a broad range of humidity levels.[32-40] The cooling power generation could be sustained through repeated atmospheric water sorption/desorption cycles.[41-43] Consequently, emerging hygroscopic coatings (i.e., hydrogels and Ionogels) designed for adsorption−evaporation cooling have primarily been applied to the rear surfaces of solar cells. These materials focus on synergistically optimizing capacity, kinetics, stability, cooling power and large-scale fabrication, while also exploring the integrated benefits for water, electricity and food production.[44-54]

Despite recent progress, considerably less attention has been paid to the spectral tuning and layer control of hygroscopic membranes, since most adsorption−evaporation cooling materials remain bulk, porous, or opaque based on a single-layered design.[21] In contrast, multilayered thin films for radiative cooling, typically installed on the sun-facing sides of solar cells, offer high transparency with precise spectral regulation.[18] However, the radiative cooling capacity is constrained by theoretical maximum cooling power (~150 W m^{-2}) and climatic conditions. To overcome the limitations of individual mechanisms, emerging research efforts have been devoted to combining evaporative and radiative cooling for enhancing atmospheric water harvesting[55-60] or daytime passive cooling for fabrics and electronics[20,61-68]. This synergistic approach simultaneously leverages both ambient humidity and cold universe as thermal sinks, thereby enhancing passive cooling efficiencies.[69] Nevertheless, this hybrid mechanism remains underexplored in the context of boosting heat dissipation and photovoltaic efficiencies of solar panels, particularly when integrating it as transparent surface plates atop solar panels.[70]

Integrating evaporative and radiative cooling onto solar systems presents a significant challenge. Specifically, multi-layered thin films applied onto solar panels for radiative cooling should maintain high transmittance and low reflectance in the absorption bands (0.3 − 1.2 μm) of

specific solar cells, while also achieving high emissivity in the mid-infrared (MIR) wavelength range (8 − 13 μm).[18] Meanwhile, fine-tuning the spectral properties and thicknesses of hygroscopic membranes to simultaneously enable hybrid passive cooling and enhance photovoltaic performance remains a critical hurdle. In addition, the concept of "two-sided asymmetry" is crucial for optimizing multiple interfaces within solar cells and passive cooling films.[71] Specifically, the development of adhesion−antiadhesion or hydrophilic−hydrophobic properties, which preserve film-device integrity and prevent accumulation at the air-film interface, is particularly intriguing. To the best of our knowledge, the concept of "Janus" structures/functions for hybrid passive cooling in solar systems has yet to be reported. Furthermore, the integration of passive cooling films on the front surfaces of electronics broadens their applicability those requiring flexibility, visual transparency and aesthetic appeal (i.e., semitransparent solar cells, wearable electronics, displays and windows). With these critical design factors in mind, the development of "self-contained" passive cooling films — integrating hybrid cooling mechanisms, spectral control, interfacial asymmetry and mechanical robustness — remains a significant challenge, yet holds great promise for advancing thermal management technologies across diverse applications.

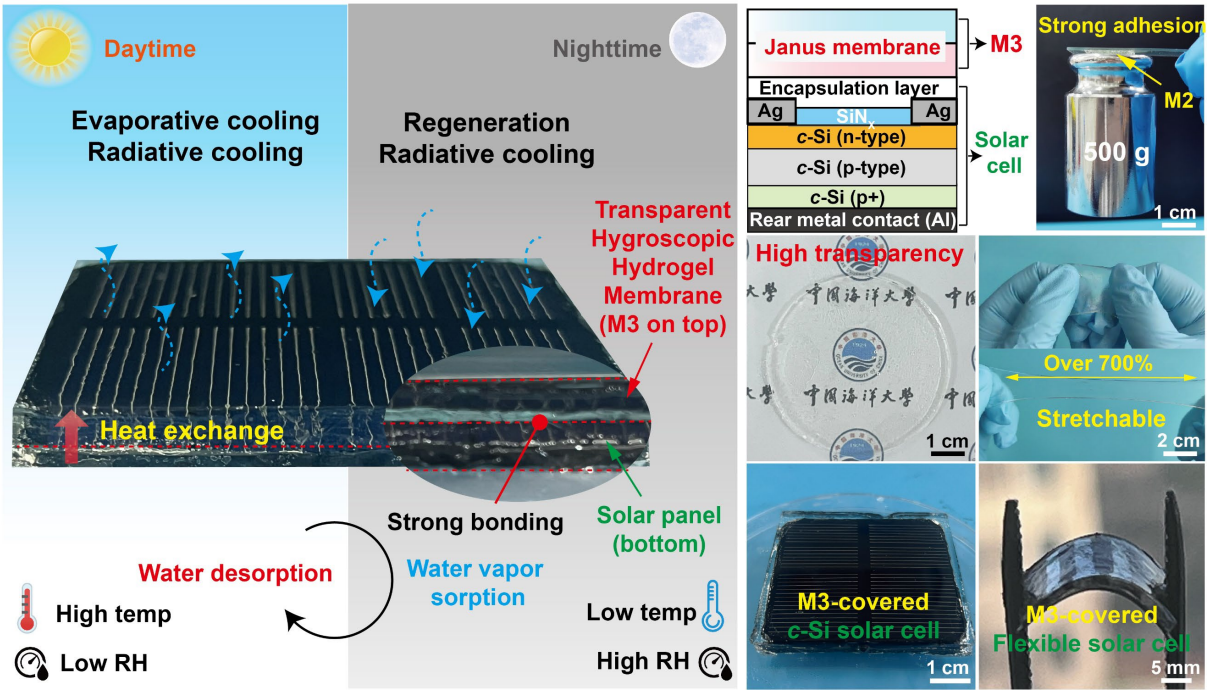

Figure 1. Schematic illustration, digital photographs and self-contained properties of hygroscopic hydrogel membrane (M3) applied onto *c*-Si (inorganic) and flexible (organic) solar cells for hybrid passive cooling effects.

In this contribution, hygroscopic hydrogel membranes were developed as surface plates through synergistic engineering of polymer components, cross-linking networks, hygroscopic salt contents and surface asymmetry. The hygroscopic salt-embedded hydrogel integrated both highly cross-linked and highly entangled networks within a precisely controlled two-layered structure. This dual-layered design preserved the high transparency, hygroscopicity and salt solution absorption in both layers, while ensuring the structural integrity, mechanical strengths and durability (**Figure 1**). The distinct polymeric networks and hygroscopic salt contents in each layer endowed Janus-like functions, enabling directional water diffusion and adhesive−antiadhesive surfaces on solar panels. The salt-in effect from highly concentrated zwitterionic polymers and large-volume swelling of the hydrogels ensured high hygroscopic salt contents (max. 20 wt%) and significantly prevented LiCl leakage, leading to reliable moisture sorption/release for effective evaporative cooling. Furthermore, this membrane provided a high transmittance (~90%) window for the absorption bands of solar cells, and also

achieved high emissivity (~98%) for sky radiative cooling. Both indoor and outdoor experiments demonstrated the hybrid passive cooling mechanism, effectively reducing surface temperatures (max. 12.1 °C) and increasing solar power output (max. 21.3%) during the daytime, while facilitating atmospheric water sorption and cooling power regeneration at night. Moreover, the cooling capability, transparency, flexibility and integrability of this membrane were demonstrated in emerging photovoltaic technologies, expanding its great potential for moisture, heat and visual regulation in various electronics. These "self-contained" functions and hybrid cooling mechanisms distinguish this hydrogel membrane from a variety of passive cooling materials used for solar panels and other electronics.

2. Results and discussion

2.1 Fabrication and characterization of two-layered hygroscopic membranes (M3)

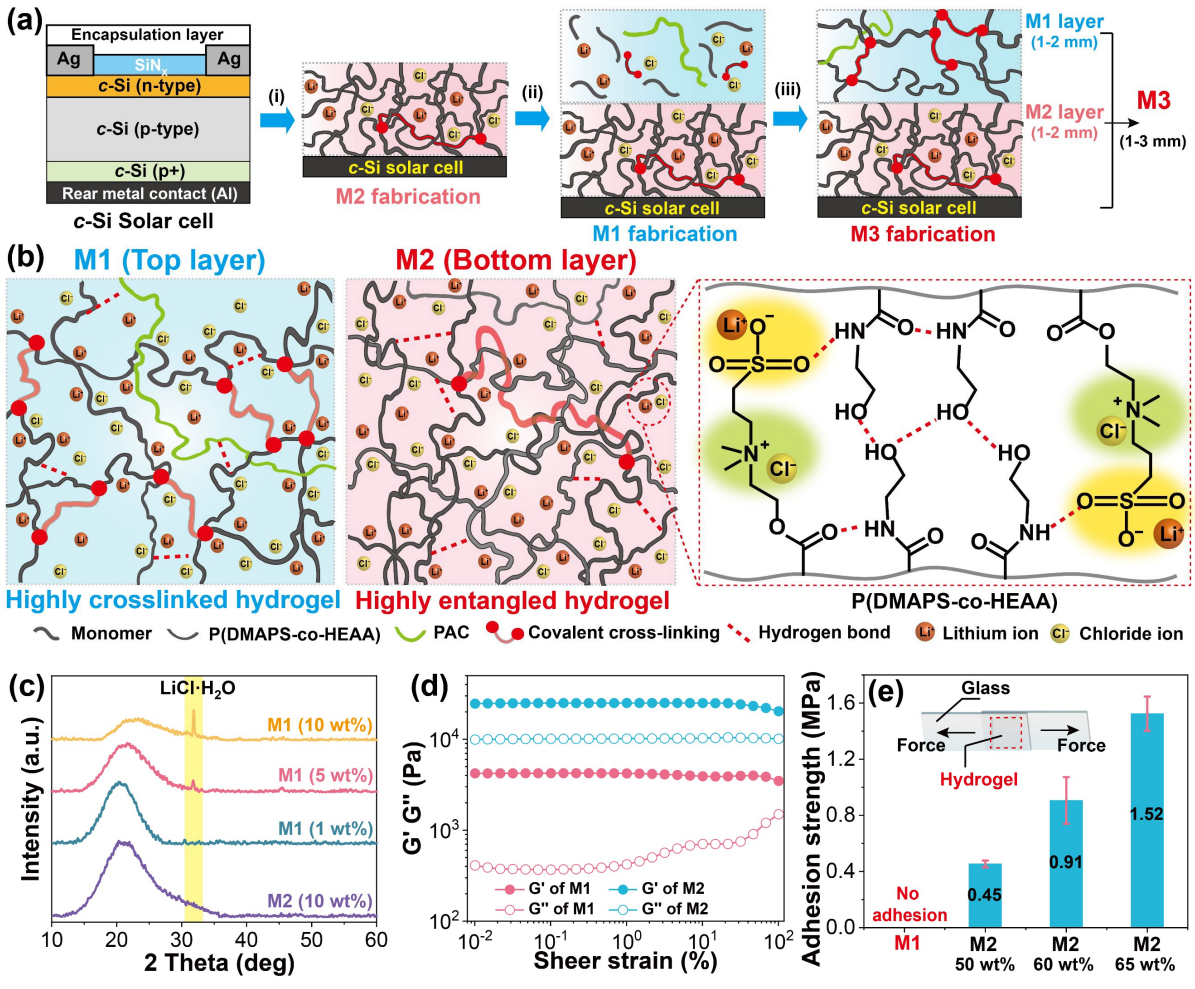

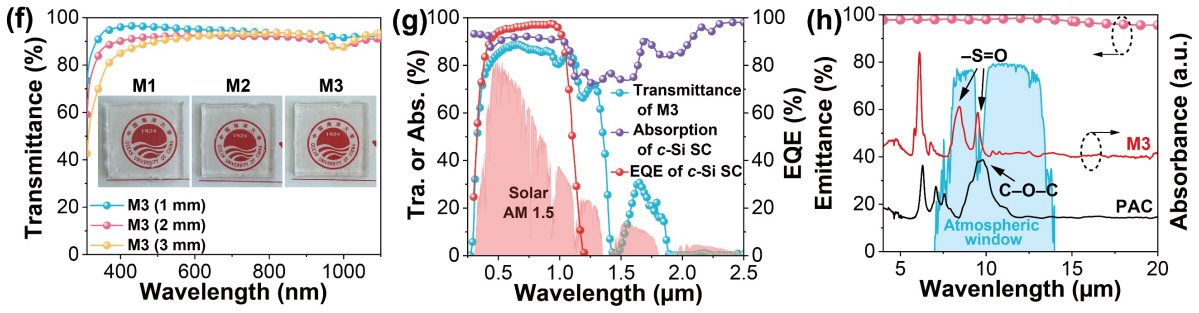

Figure 2. (a) Flowchart of the fabrication of the two-layered hygroscopic membrane (M3) integrated onto a *c*-Si solar cell. (b) Design strategies, cross-linking networks and chemical structures of the top (M1) and bottom (M2) layers within M3. (c) XRD patterns of M1 and M2. (d) G′ and G″ of M1 and M2 under strain sweep. (e) Adhesion strengths of M1 and M2. (f) Transmittance of M3 with different thicknesses. (g) Absorptance and EQE spectra of *c*-Si solar cell. (h) Emittance and absorbance spectra of M3.

The fabrication flowchart of the two-layered hygroscopic membrane (denoted as M3) is illustrated in **Figure 2a**. A monocrystalline silicon-based (*c*-Si) solar cell (50 × 50 mm^2) with a passivated emitter rear contact (PERC) structure and protective encapsulation was employed. The *c*-Si layer absorbed incident light, generating an electric current that was directed to the metal electrodes. M3 (1 − 3 mm) was fabricated atop the *c*-Si solar cell through a two-step procedure. The bottom hydrogel layer (denoted as M2, 1 − 2 mm) was engineered to optimize adhesion, water retention and transparency, and was initially fabricated onto the encapsulation layer (glass) of the *c*-Si solar cell. The top hydrogel layer (denoted as M1, 1 − 2 mm) was designed for water vapor sorption, salt solution absorption and transparency with minimal adhesion. M1 was subsequently fabricated atop M2, forming two-layered structure with Janus properties.

Initially, a copolymer (denoted as P(DMAPS-*co*-HEAA)) was synthesized from [2-(methacryloyloxy)ethyl]dimethyl-(3-sulfopropyl)ammonium hydroxide (DMAPS) and (2-hydroxyethyl)acrylamide (HEAA) monomers, serving as the fundamental building block for both M1 and M2 (Figure S1, Supporting Information). The DMAPS units featured an equal

number of anionic and cationic groups on their side chains, forming a zwitterionic structure that induced a "salt-in" effect with lithium chloride (LiCl). Such zwitterions within the copolymers facilitated the binding of Li^+ and Cl^- ions through coordination, effectively mitigating LiCl leakage. The variations in LiCl contents also modulated the osmotic pressure and swelling of the hydrogels for LiCl solution absorption and retention. In addition, the amphipathic HEAA units, with numerous hydrogen bond donor and acceptor sites, contributed to both interfacial adhesion and intrinsic cohesion of the hydrogels. To prepare the precursor solutions, all DMAPS and HEAA monomers were dissolved in LiCl solutions, followed by UV-assisted free-radical polymerization. The viscous precursor solutions were blade-coated onto substrates and subjected to layer-by-layer UV curing, yielding self-standing two-layered hydrogel membranes with millimeter-scale thicknesses precisely controlled. After fabrication on solar cells, all as-prepared hydrogel membranes (M1, M2 and M3) were used for water vapor sorption without prior dehydration. Nuclear magnetic resonance (NMR) spectroscopy confirms the successful copolymerization of the DMAPS and HEAA monomers, resulting in a series of random polymers. The composition of the two segments within the copolymers closely matched the initial monomer ratio (Figure S2, Supporting Information).

Although the same monomers were used in both M1 and M2, variations in the mass concentrations of monomers, cross-linkers and initiators resulted in distinct cross-linking networks. These variations endowed M1 and M2 with Janus structures and functionalities, highlighting the structural differences between their respective cross-linking networks, as illustrated in **Figure 2b**. For M2, the incorporation of LiCl significantly improved the solubility of the DMAPS monomer through the salt-in effect, enabling its concentration to exceptionally high weight ratios (65 wt%) in LiCl solutions. A limited initiator-to-monomer molar ratio (4.0×10^{-5} : 1) and a minimal cross-linker-to-monomer molar ratio (1.0×10^{-4} : 1) led to the formation of a "highly entangled" polymer network within M2. In this network, polymer

entanglements vastly outnumber cross-links, with interactions primarily driven by polymer chain entanglement rather than covalent or non-covalent bonding.[64,72-73] To identify optimal M2, a series of highly entangled polymers (denoted as H1 − H9) were synthesized with varying total concentrations, chemical compositions and LiCl contents, as detailed in Table S1, Supporting Information. A cyclic compression test demonstrated that, compared to the hydrogels with lower polymer ratios (H1: 50% and H2: 60 wt%), increasing the total polymer ratio to 65 wt% (H7) resulted in the highest compressive stress (over 230 kPa) and the lowest plastic deformation (below 28%), with both properties retained over 100 load−unload cycles (Figure S3, S4 and S5, Supporting Information). Furthermore, tensile testing reveals that M2 (H7) attained a significantly high tensile strength of 10.5 MPa and an exceptional fracture strain (elongation at break) of 787.3% (Figure S6 and Video S1, Supporting Information). These mechanical measurements reveal exceptional toughness, strength, elasticity and fatigue resistance generated by the highly entangled polymer networks. In addition, the LiCl contents (H3, H4 and H7) were varied from 5 to 10 wt%, relative to the total mass of the hydrogels. Water vapor sorption characterization revealed that H7 (size: 15 mm × 15 mm × 3 mm) with 10 wt% LiCl achieved the highest water uptake of 268.6 g m^{-2} under 90% relative humidity (RH) after 24 h (Figure S7a, Supporting Information). It is noted that LiCl contents exceeding 10 wt% could not be readily dissolved, owing to the limited water contents (25 − 40 wt%) in these highly entangled hydrogels (H1 − H9). Furthermore, by fixing the total weight ratio at 65 wt% and the LiCl content at 10 wt%, the molar ratios of DMAPS to HEAA were modulated from 2:1 to 1:2 in H6 − H8. Highly entangled hydrogels composed of neat DMAPS or HEAA monomers were also synthesized as control groups, yielding H5 and H9, respectively. The cyclic compression and water vapor sorption were systemically evaluated. Among all these hydrogels (H1 − H9), the highly entangled hydrogel with a DMAPS:HEAA molar ratio of 1:1 (H7) synergistically achieved superior compression strength, deformation resistance, durability

and water vapor sorption (Figure S7b, Supporting Information). As a result, the DMAPS to HEAA molar ratio was set at 1:1 for the fabrication of all layers in M1, M2 and M3.

M1 was a conventional hydrogel with a low polymer concentration of 20 wt% in total. Unlike M2, the increased initiator-to-monomer molar ratio (1.4%) and cross-linker-to-monomer molar ratio (0.3%) used for polymerization led to a "highly cross-linked" network within M1. Polyanionic cellulose (PAC) was incorporated as a secondary polymer component, forming a semi-interpenetrating network in M1 (Figure S8, Supporting Information). The cellulose backbones with C−O−C and C−O bonds exhibit characteristic absorbance and high emissivity in the MIR spectrum ($\lambda \approx 8 - 13$ μm), rendering cellulose-based porous structures a promising structural component for sky radiative cooling.[74-75] Furthermore, the high water solubility of PAC ensured M1's high transparency. Owing to the highly increased water-to-monomer molar ratio (32.2 : 1) in M1 compared to M2 (4.2 : 1), the LiCl content in M1 can be elevated from 10 to 20 wt% (relative to the total mass of the hydrogels), thereby leading to a significant increase in water uptake from 92.0 to 222.7 g m^{-2} under 90% RH after 24 h (Figure S9, Supporting Information). However, compared to highly entangled M2, the semi-interpenetrating network with extensive cross-linking embrittled M1, reducing its tensile strength (1.0 MPa) and fracture strain (226.0%). Upon integrating M1 onto M2, the tensile strength and fracture strain of M3 (comprising 1.5 mm of M1 and 1.5 mm of M2) were found to lie between those of M1 and M2 (Figure S6, Supporting Information). During tensile testing, the M1 layer in M3 initially fractured, while the M2 layer remained intact, resulting in M3 exhibiting a high fracture strain (519.0%) before failure. This result discloses that the mechanical strength, elastic modulus, toughness and fracture strain of the two-layered hydrogel (M3) can be enhanced by incorporating the highly entangled hydrogel (M2) with the conventional hydrogel (M1), highlighting one of the key advantages of the two-layered design.

X-ray diffraction (XRD) patterns revealed that LiCl predominantly existed as ion pairs bonded

to zwitterions in M1 when the LiCl content was as low as 1 wt% (**Figure 2c**). Notably, the characteristic crystal peak of LiCl monohydrate ($LiCl·H_2O$) emerged when the LiCl contents increased to 5 and 10 wt%, indicating the presence of LiCl monohydrate in M1. The DMAPS units with a common concentration of 14.2 wt% in M1 were unable to ionically bond with 20 wt% of LiCl, resulting in the presence of free LiCl monohydrate. In contrast, the significantly higher concentration (46 wt%) of the DMAPS units in M2 effectively inhibited LiCl crystallization, even at a LiCl content as high as 10 wt%. Nearly all LiCl was ionically bound to the zwitterions, with no discernible crystal peak corresponding to the monohydrate phase, indicating the significant potential to prevent LiCl leakage from M2.

The storage modulus (G') and loss modulus (G") of M1 and M2 are plotted as a function of shear strain (**Figure 2d**). G′ represents the hydrogel's capacity to store elastic energy, while G″ quantifies its ability to dissipate energy during deformation. Notably, both G' and G" values for M2 were consistently higher than those of M1 across a broad shear strain range from 1‰ to 100%. The higher G′ values of M2 indicate enhanced stiffness and toughness, which contribute to its resistance to deformation and maintain structural integrity under stress. Moreover, the increased G″ values of M2 reflected a more pronounced viscous behavior, facilitating more efficient energy dissipation during deformation.

Adhesion experiments of M1 and M2 were conducted using a lap shear test. A glass slide (25.4 × 76.2 × 2 mm^3) was used as the substrate, onto which a square sample square sample (15 × 15 mm^2) was placed. Another glass slide was positioned atop the sample to form an adhesive joint with an overlapping area of 225 mm^2. The measurements were conducted on five patches for each hydrogel and adhesion strengths are summarized in **Figure 2e**. M1 exhibited negligible adhesion to glass, whereas M2 formed a strong bond, indicating a Janus-like adhesion. The adhesion strengths of the M2/glass joints increased from 0.45 to 1.52 MPa as the total polymer concentration was increased from (H1) 50 wt% to (H7) 65 wt%. The best-performing adhesive

joint was able to support a weight of 500 g (**Figure 1**). The adhesion mechanism of M2 on glass can be explained as follows: i) The surface groups on the glass provided multiple bonding sites for the DMAPS and HEAA units, enabling a variety of interfacial interactions, including electrostatic interactions, hydrogen bonds, ion−dipole interactions and van der Waals interactions (Figure S10, Supporting Information). These interactions facilitated strong interfacial bonding within the M2/glass adhesive joint. ii) The high polymer concentration (65 wt% in total) facilitated the formation of interfacial bonding sites, polymer chain entanglement and noncovalent (i.e., hydrogen bonds) cross-linking within M2, synergistically enhancing its adhesion and cohesion. These results demonstrate a Janus-like adhesion between the top and bottom surfaces of M3: the negligible adhesion of M1 ensured an antifouling property to the M3 surface, preventing dust accumulation, while the strong adhesion of M2 ensured the secure attachment and conduction pathway of M3 onto the encapsulation glass of solar cells (Video S2, Supporting Information), highlighting another key advantage of the two-layered design.

In addition to glass films, polyethylene terephthalate (PET) and ethylene-vinyl acetate (EVA) are promising synthetic polymers for encapsulating of next-generation solar cells. To evaluate interfacial compatibility, additional adhesion experiments were conducted on PET and EVA substrates using an identical lap shear test (Figure S11, Supporting Information). M1 exhibited negligible adhesion to both PET and EVA. On the other hand, the average adhesion strengths of the M2/PET and M2/EVA joints were 0.20 and 0.35 MPa, respectively. This result indicates the broad applicability of the Janus adhesion design across diverse surfaces.

Optical properties of single- and dual-layered hydrogel membranes were studied. Both M1 and M2 featured high transmittance in the visible and NIR wavelength regions (300 − 1100 nm) (Figure S12, Supporting Information). M1, with varying thicknesses of 1, 2 and 3 mm, afforded effective transmittance of 92.3%, 89.9% and 87.5%, respectively. Similarly, M2 with thicknesses of 1, 2, and 3 mm exhibited effective transmittance of 94.1%, 90.7% and 87.7%,

respectively (Section S11, Supporting Information). When incorporated into M3 with identical thicknesses for M1 and M2, M3 afforded effective transmittance of 92.3%, 90.0% and 87.7% for thicknesses of 1, 2 and 3 mm, respectively (**Figure 2f**). The high transmittance of M3 well agrees with the pronounced absorption of the *c*-Si layer across 300 − 1100 nm,[14] establishing an effective sunlight absorption window for *c*-Si solar cells. Although a slight decrease in transmittance was observed with increasing thickness of M3, its water uptake capacity significantly improved as the thickness increased (Figure S13, Supporting Information). Quantitatively, this transmittance−hygroscopicity trade-off was partially mitigated in M3 with a thickness of 3 mm. In this case, a high water uptake of 282.22 g m^{-2} was achieved under 90% RH after 24 h, while retaining a high average transmittance greater than 91% across the 450 − 950 nm range.

Table 1. Summary of key parameters for M1 and M2.

Parameters	M1	M2
Polymer concentration (wt%) [a]	20	65
Cross-linker−to−monomer ratio [b]	0.3 : 100	1.0×10^{-4} : 1
Initiator−to−monomer ratio [b]	1.4 : 100	4.0×10^{-5} : 1
LiCl content (wt%) [a]	20	10
Water−to−monomer ratio [b]	32.2 : 1	4.2 : 1
Tensile strength (MPa)	1.0	10.5
Fracture strain (%)	226.0	787.3
Water uptake (g m^{-2}) [c]	222.7	268.6
Transmittance (%) [c,d]	91.2	91.9
Adhesion strength (MPa) [e]	None	1.52

[a] mass ratio relative to total hydrogel, [b] molar ratio, [c] the thickness of the hydrogel is 3 mm, [d] average transmittance in the 450 − 950 nm range, and [e] on glass substrates

Main parameters (i.e., material components, reagents mechanical properties, water uptake, transmittance and adhesion) for the fabrication and characterization of M1 and M2 are summarized in **Table 1**. After systematically evaluating the material components, optical

transmittance, hygroscopic capacity and mechanical properties of the dual layers, 3 mm M3, comprising 1.5 mm of M1 and 1.5 mm of M2, was selected as the optimal hydrogel membrane for further studies on water vapor sorption/desorption, solar energy conversion and passive cooling properties.

The reflectance and transmittance of the *c*-Si solar cell were also measured. The absorptance was calculated as 1 − T − R, where T and R represented transmittance and reflectance at the same wavelength, respectively. The absorptance spectrum of the *c*-Si solar cell ranged from 250 − 2500 nm, encompassing all photons absorbed for both light-to-electricity and light-to-heat conversion. External quantum efficiency (EQE) is defined as the ratio of free charge carriers extracted from a solar cell to the flux of incident photons. The EQE spectrum of the *c*-Si solar cell demonstrated that light-to-electricity conversion primarily occurred in the wavelength range of 290 − 1200 nm, which closely matched the absorption spectrum of the *c*-Si layer.[14] This EQE band was entirely within the main transmission band of M3 (270 − 1450 nm), indicating that M3 had a negligible impact on limiting sunlight absorption and photo-to-electricity conversion of *c*-Si solar cells. On the other hand, the transmission of M3 sharply decreased in the 1450 − 2500 nm wavelength range, effectively blocking the majority of NIR photons. These photons did not contribute to photo-to-electricity conversion and instead heated the solar panels.

To evaluate the radiative cooling effect, the emissive spectrum of M3 was measured across the MIR wavelength range (4 − 20 μm) (**Figure 2h**). M3 exhibited an average emissivity of ~98.1% in the atmospheric transparent window (8 − 13 μm), ensuring efficient heat dissipation to deep space. The hydrated state in as-prepared M3 and the high emissivity of water molecules, played a critical role in broadening the IR emittance of M3. Similar enhancements in IR emittance have been observed in water-containing fabrics and aerogels used for radiative cooling and heat stress dissipation.[58] The high emissivity of M3 can be partially attributed to the multimode

vibrations of functional groups, including C−O−C stretching in the PAC backbones and −O=S stretching in the DMAPS units, both of which exhibited IR absorptions within the atmospheric transparency window.[20,74-75] The high and broad emissivity of M3 enabled this hydrogel membrane to effectively dissipate heat from solar cells during the daytime through radiative cooling. Furthermore, the radiative cooling effect could lower the pressure of water vapor and enhance condensation, improving water vapor sorption and regeneration of M3 at night. In brief, the two-layered structure in M3 preserved the high transparency, hygroscopicity and water retention of both layers, while ensuring the structural integrity. Moreover, two-layered structure exhibited distinct polymeric networks, LiCl contents, adhesion strengths and mechanical properties, and these Janus-like features facilitate optical properties and hybrid passive cooling mechanisms tailored for solar cells.

2.2 Water Vapor Sorption and Desorption

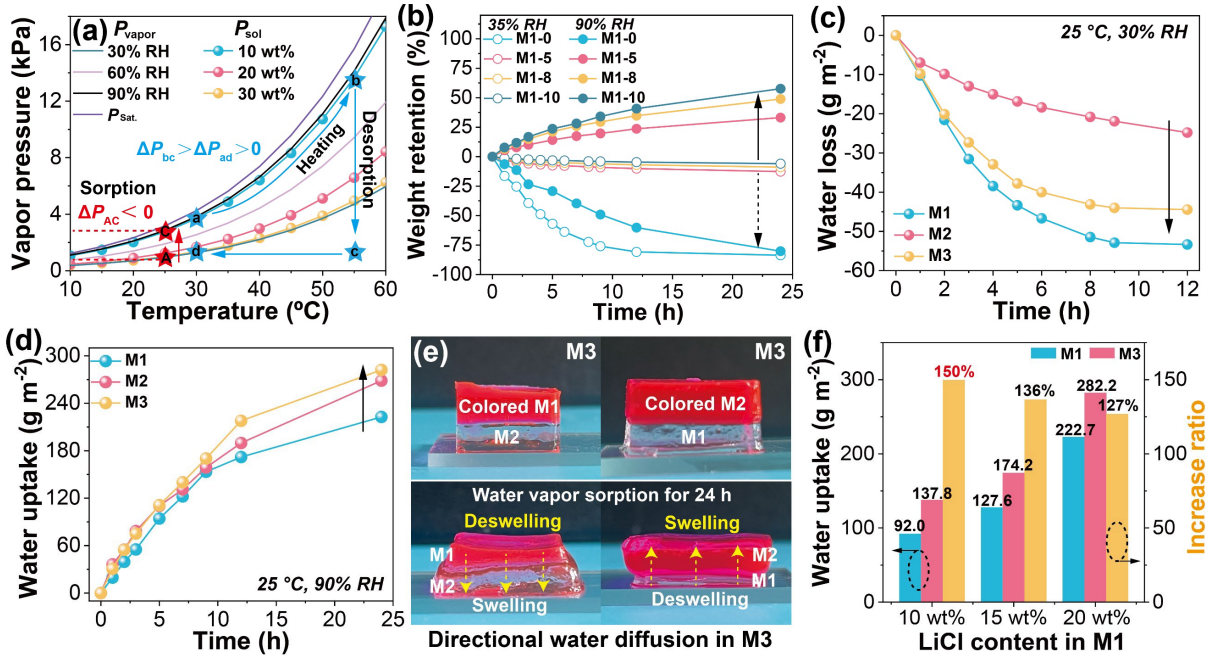

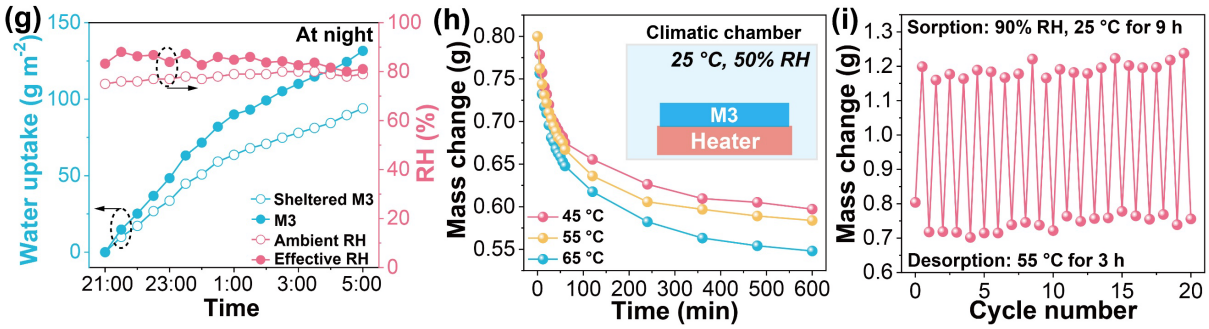

Figure 3. (a) P_{vapor} under different RHs and ambient temperatures, and P_{sol} of different LiCl solutions under varying ambient temperatures. (b) Normalized weight changes of M1 with different LiCl contents variation during water vapor sorption/desorption. (c) Deswelling properties and normalized weight changes of M1, M2 and M3 under low RH. (d) Water vapor sorption of M1, M2 and M3 under 90% RH and at 25 °C. (e) Osmotic pressure-driven water diffusion and anisotropic swelling within M3. (f) Summary of water uptake of M1 and M3 with different LiCl contents under 90% RH and at 25 °C. (g) Ambient RH, effective RH and water vapor sorption of M3 under outdoor conditions over night. (h) Heat-induced water desorption of M3. (i) Water uptake and release characterization of M3 in 20 moisture sorption−desorption cycles.

RH is defined as the ratio of the partial pressure of water vapor (P_{vapor}) in air to the saturation pressure ($P_{sat.}$). P_{vapor} accounts for both ambient RH and temperature.[76] The correlation between P_{vapor} and temperature at different RH levels is illustrated in **Figure 3a** (lines). The upper curve (purple line) corresponds to the saturation pressure ($P_{sat.}$) at 100% RH, representing the saturation curve where condensation occurs. Unsaturated air can reach saturation by cooling or increasing the absolute humidity. Notably, the M1 and M2 layers in M3 were fabricated through degassing followed by polymerization of precursor solutions, resulting in LiCl-embedded hydrogels with a solid, non-porous structure. This structural characteristic distinguishes M3 from conventional hygroscopic salt-embedded aerogels and foams, which rely on hierarchically porous networks to enhance LiCl contents and salt solution absorption via pore-confinement or capillary effects. In contrast, water vapor sorption/desorption in M3 occurred exclusively at the hydrogel/air interface, resembling the sorption/desorption at the solution/air interface of LiCl solutions. This observation suggests a unique mechanism

governing moisture uptake, diffusion and LiCl solution retention in M3.

During water vapor sorption, the moisture sorption and desorption of LiCl solutions within hydrogel membranes are governed by their vapor pressure (P_{sol}), which depends on the thermodynamic properties of the solutions, including LiCl concentrations and temperatures (Section S13 and Table S2, Supporting Information). The relationship between P_{sol} and temperature across different RH levels is presented in **Figure 3a** (point plot). In this case, water vapor sorption by LiCl solutions is primarily driven by the gradient between P_{vapor} and P_{sol}. Water vapor sorption ceases when P_{sol} reaches equilibrium with P_{vapor} under specific RH and temperature.[77] For example, when a 30 wt% LiCl solution (denoted as red point A) was exposed to a humid environment at 25 °C with 90% RH (denoted as red point C). The P_{vapor} difference ($\Delta P_{AC} < 0$) can drive spontaneous water vapor sorption from this LiCl solution, leading to its volumetric expansion and dilution. As the LiCl concentration in the solution decreased from 30 wt% to 10 wt% through moisture sorption, the increase in P_{sol} significantly diminished the driving force (ΔP), thereby lowering the equilibrium sorption capacity and kinetics of the solution.

For water desorption, when a 10 wt% LiCl solution (high P_{sol}, denoted as blue point a) was exposed to an environment with 30% RH and 30 °C (low P_{vapor}, denoted as blue point d), the P_{vapor} difference ($\Delta P_{ad} > 0$) can drive spontaneous water desorption from the LiCl solution. When the LiCl solution was warmed from 30 to 55 °C, the P_{vapor} difference further increased significantly from ΔP_{ad} to ΔP_{bc}, thereby facilitating water desorption. Importantly, the thermal energy required for desorption can be harnessed from low-grade or sustainable energy sources such as sunlight or waste heat. As a result, the LiCl concentration, along with the RH- and temperature-dependent difference between P_{vapor} and P_{sol} play a critical role in regulating moisture sorption and desorption, specifically through deliquescence and solution absorption stages within the hydrogel membranes.

To validate the proposed hypothesis, a series of water vapor sorption/desorption experiments were performed on single- and dual-layered hydrogel membranes. Different M1 samples with varying LiCl contents (0 wt%, 5 wt%, 8 wt% and 10 wt%) were prepared and designated as M1-0, M1-5, M1-8 and M1-10, respectively. To ensure consistency, all hydrogel membranes were tailored to identical dimensions (15 × 15 × 3 mm^3) and water vapor sorption occurred exclusively at the M1/air interfaces. Each M1 sample was exposed to 35% RH (low) or 90% RH (high) at 25°C, with water gain and loss monitored over 12 − 24 h (**Figure 3b**). Under high RH, the P_{vapor} value in air exceeded those of M1-5, M1-8 and M1-10, leading to water vapor sorption and subsequent weight gain. Among these, M1-10 exhibited the highest negative P_{vapor} difference, resulting in the fastest sorption and the most significant increase in water content (57.7%) after 24 h. On the other hand, M1-0, which contained no LiCl, experienced spontaneous water loss under both low and high RH conditions, attributed to the positive P_{vapor} differences. At low RH, where the positive P_{vapor} difference was maximized, M1-0 demonstrated the fastest water loss, reaching equilibrium after 12 h and exhibiting an 80.8% weight loss after 24 h. As the LiCl contents in M1 increased, the P_{vapor} differences gradually diminished, resulting in a reduction in water loss. Specifically, M1-5, M1-8 and M1-10 exhibited weight losses of 12.6%, 8.9% and 5.9% after 24 h, respectively. These results demonstrate that water vapor sorption and desorption in the hydrogel membranes can be controlled by the sign and magnitude of the P_{vapor} difference, which directly influences the quantity and dynamics of water uptake and release.

Water vapor sorption/desorption experiments of M1, M2 and M3 (15 × 15 × 3 mm^3) were conducted based on optimized LiCl contents and structural configurations. To ensure consistency in comparison, the mass fraction of LiCl was defined as the ratio of the weight of LiCl to the total mass of both LiCl and water in each hydrogel membrane. The LiCl mass fractions in M1, M2 and M3 were calculated and determined to be 25.4%, 28.6% and 26.4%,

respectively. Under 30% RH and at 25°C, M1, M2 and M3 exhibited spontaneous water loss and reached equilibrium states after 12 h (**Figure 3c**). The lowest LiCl fraction in M1 maximized the P_{vapor} difference, leading to its largest water loss of 53.4 g m^{-2} after 12 h. As the LiCl fraction increased, the water loss decreased gradually, with M3 exhibiting a moderate water loss at 44.4 g m^{-2} and M2 reaching the lowest water loss at 24.8 g m^{-2} after 12 h. This result demonstrates that the LiCl mass fractions in these hydrogels inversely correlate with their water loss and desorption dynamics under low RH conditions, which agree well with the data presented in Figure 3a and 3b.

Under 90% RH and at 25 °C, M1, M2 and M3 exhibited spontaneous water vapor sorption over time (**Figure 3d**). M1 absorbed 222.7 g m^{-2} of water after 24 h, while M2 exhibited a higher water uptake of 268.6 g m^{-2}. This trend aligns well with the LiCl fractions and the corresponding P_{vapor} differences in M1 and M2, suggesting that the water uptake of M3 should fall between that of M1 and M2. However, the water uptake of M3 significantly exceeded those of both M1 and M2, reaching 282.22 g m^{-2} after 24 h. These results disclose that the overall water uptake of the hydrogel membranes was not solely governed by the LiCl concentrations and environmental parameters through water vapor sorption mechanisms, but also by other limiting factors, such as water diffusion and volumetric expansion (swelling).

In solid hydrogels (M1 and M2), water diffusion is primarily driven by osmotic pressure gradients rather than surface tension within capillaries. The inherent swelling behavior of these hydrogels promotes water diffusion and salt solution absorption, while potentially preventing salt solution leakage. For M3, its two-layered structure and the variations in LiCl concentrations across layers could create an osmotic pressure gradient, enabling directional water diffusion throughout M1 and M2. A series of experiments were conducted to evaluate the osmotic pressure differences and the resulting water diffusion in M1 and M2. Water contact angle tests were employed to quantify the time required for water droplet absorption by M1 and M2 (Figure

S14, Supporting Information). The M1 surface completely absorbed the water droplet within 2 s, while the M2 surface the M2 surface exhibited a longer absorption time within 60 s. Furthermore, the osmotic pressure of each hydrogel was quantified by immersing it in solutions of varying LiCl concentrations until thermodynamic equilibrium was reached. When no clear swelling occurred in a specific LiCl solution, the osmotic pressure of that solution was considered to be in equilibrium with the hydrogel's osmotic pressure. Swelling experiments were conducted for M1 and M2, with their swelling ratios measured over time (Figure S15, Supporting Information). Both M1 and M2 exhibited clear swelling in LiCl solutions across a broad concentration range (20 − 40 wt%). M1 afforded an average swelling ratio of ~4.5 g g^{-1} in these solutions, while a significantly higher swelling ratio of ~21.4 g g^{-1} was observed from M2. According to Flory-Rehner theory, the equilibrium swelling ratio of a hydrogel is generally determined by the balance between the osmotic pressure arising from the polymer-solvent mixing free energy and the network elasticity within the hydrogel.[78] The smaller swelling ratio observed for M1 could stem from the shorter polymer chains generated by its highly cross-linked network, compared to M2.

Fitting to the Fickian diffusion model, the diffusive permeability (D_w) of 20 − 40 wt% LiCl solutions throughout M1 and M2 was evaluated based on the swelling measurements, which ranged from 6.15×10^{-13} to 1.10×10^{-9} m^2 s^{-1} (Figure S16, Supporting Information). This range falls within the reported values for various hydrogels and is lower than the self-diffusion coefficient of neat water (2×10^{-9} m^2 s^{-1}),[79] confirming the diffusion-govern water transport in M1 and M2. Furthermore, the absorption fluxes of M1 and M2 for various LiCl solutions (20 − 40 wt%) were estimated (Figure S17, Supporting Information). Over the first 3 h, the average absorption flux of M1 gradually decreased from 0.15 to 0.03 LMH, while M2 exhibited a decrease from 0.26 to 0.05 LMH. Concurrently, the osmotic pressure of the LiCl solution gradually increased from 252.1 atm (20.0 wt%) to 538.5 atm (40 wt%). The osmotic pressure

differences between the hydrogels and LiCl solutions decreased over time, thereby reducing the average absorption fluxes.[79] Compared to M1, M2 afforded higher absorption fluxes across a wide osmotic pressure range, indicating its superior LiCl solution absorption. Although the osmotic pressure of M1 and M2 cannot be directly measured due to the solubility limit of LiCl in water (~45.5 wt% at 20 ℃), the osmotic pressure of both M1 and M2 is estimated to exceed that of a highly concentrated LiCl solution (538.5 atm for 40 wt% LiCl solution). Notably, this osmotic pressure is significantly higher than the capillary pressure of macropores (~1 μm) and remains independent of pore size and flow resistance. This behavior contrasts with viscous flow in capillaries.[79]

Driven by the osmotic pressure gradient, the directional water diffusion occurred between M1 and M2 when placed together (**Figure 3e**). These dual layers (15 × 15 × 10 mm^3) were placed under 90% RH and at 25°C, with either the M1 or M2 layer (15 × 15 × 5 mm^3) stained with rhodamine B to visualize the distinct deformation resulting from swelling and deswelling. When the M1 layer was oriented upwards, water absorbed by its surface spontaneously diffused into the M2 layer, resulting in significant swelling of M2. Conversely, when the M2 layer faced upwards, the absorbed water remained primarily within M2, rather than diffusing into M1. Notably, the water in M1 exhibited anti-gravitational diffusion toward the M2 layer, causing a noticeable shrinkage of M1. This observation is in good agreement with the swelling and osmotic pressure characterization, which visualized the directional water diffusion.

When exposed to 90% RH, the surface layer (M1) of M3 spontaneously absorbed water, driven by the P_{vapor} difference at the M1/air interface. Increasing the LiCl content in M1 from 10 to 20 wt% amplified this P_{vapor} difference, leading to a significant enhancement in the overall water uptake of M3 from 137.78 to 282.22 g m^{-2} after 24 h (**Figure 3f**). However, as the LiCl content in the M1 layer increased, the osmotic pressure gradient responsible for directional water diffusion from M1 to M2 decreased. Although the water uptake of both M1 and M3 increased,

the increase ratio (defined as the ratio of M3's water uptake relative to M1) gradually declined from 150% to 127%. This result discloses the synergistic interplay between water vapor sorption and liquid water diffusion, which collectively govern the total water uptake in this dual-layer hydrogel system. In brief, the high LiCl concentration (20 wt%) in M1 increased the P_{vapor} difference relative to the humid air, boosting water vapor sorption. Simultaneously, the proper osmotic pressure gradient between M1 and M2 ensured directional water diffusion from M1 to M2. Consequently, the absorbed water was effectively transferred from the surface of M3 to its interior. These results highlight one of the main advantages of this dual-layer design, which synergistically enhanced water vapor sorption, directional diffusion, LiCl solution absorption and retention within hygroscopic hydrogels.

Taking into account the optical and hygroscopic properties of M3, its passive cooling effect on solar panels synergistically combined evaporative and radiative cooling mechanisms. However, distinguishing these effects during the daytime was challenging. To isolate and evaluate radiative cooling, the surface temperature and atmospheric water sorption of M3-covered solar cells were measured at night, when evaporative cooling was negligible. A control cell, covered with a transparent poly(methyl methacrylate) (PMMA) slide to suppress radiative cooling, was also tested. Outdoor experiments were performed in March, Qingdao, China, with ambient temperature and RH recorded from 21:00 to 5:00 (Figure S18, Supporting Information). The PMMA-shielded M3/solar cell exhibited an average surface temperature ~1.0 °C above ambient, due to heat released during atmospheric water sorption by M3. On the other hand, the M3-covered solar panel afforded an average surface temperature ~0.9 °C below ambient owing to radiative cooling. This temperature reduction decreased $P_{sat.}$ of water vapor (Figure S19a, Supporting Information). Consequently, the effective RH surrounding the M3-covered solar panel was higher than the ambient RH, with a maximum difference exceeding 12% during the night (**Figure 3g**). In addition, the reduced surface temperature increased the P_{vapor} difference

between M3 and the surrounding air, thereby enhancing the driving force for moisture sorption (Figure S19b, Supporting Information). Owing to the increase in effective RH and the P_{vapor} difference, the M3-covered solar cell exhibited water uptake of 131.6 g m^{-2} over 8 h at night, resulting in a 1.4-fold increase in moisture sorption compared to the control device (94.0 g m^{-2}) during the same period. These results demonstrate the presence of a radiative cooling effect in the M3-covered solar cell, which is in good agreement with the optical properties of M3. Particularly at night, the radiative cooling effect effectively facilitated atmospheric water sorption of M3 through increasing effective RH and P_{vapor} difference.

To simulate solar-driven evaporation, water desorption of M3 was studied in a climatic chamber, where a hot plate was used to mimic varying surface temperatures (45 − 65 °C) of solar panels under sunlight (**Figure 3h**). Upon heating, the P_{vapor} difference between M3 and the surrounding air enhanced water desorption. In the first 2 h, all M3 samples (weight: 0.8 g and size: 15× 15 × 3 mm^3) exhibited rapid water release at 45, 55 and 65 °C. As LiCl within M3 became increasingly concentrated due to dehydration, the P_{vapor} gradient diminished, resulting in a gradual decrease in desorption rates. After 10 h of heating, M3 samples lost 25.0%, 27.5% and 31.3% of their initial hydrogel mass, respectively, confirming that higher temperatures enhanced water desorption. In addition, ambient RH changes (40 − 90% RH), controlled by the climatic chamber, also influenced water desorption of M3. At a fixed heating temperature of 55 °C, increasing RH markedly suppressed water desorption of M3 (Figure S20, Supporting Information).

A variety of LiCl-embedded hygroscopic composites were designed to generate multiscale hierarchical pore structures for increasing the overall LiCl contents embedded within the walls of the pores, and enhancing water-retaining capillary force for LiCl solution absorption.[77] However, rapid and control fabrication of capillary matrices are challenging to boost salt contents and water-holding capacity provided by the capillary matrices.[80] Taking the

advantages of using zwitterionic polymers within a highly entangled hydrogel, the limitation of LiCl leakage in our study adopted two meticulously designed strategies, including the salt-in effect of highly concentrated zwitterionic polymers and large-volume swelling of hydrogels in LiCl solutions. To create the salt-in effect, LiCl was directly incorporated into the DMAPS and HEAA monomers via copolymerization. This strategy screened inter- and intrachain interactions between oppositely charged groups, and facilitated the solubilization of highly concentrated DMAPS monomers, enabling the formation of a zwitterionic hydrogel with a highly entangled structure. This network effectively restricted the migration of salt ions within M2. Excluding the swelling, the presence of highly concentrated DMAPS units (46 wt%) theoretically provided a LiCl-holding capacity of ~7.0 wt% for M2. Furthermore, the concentration of the LiCl solution was determined to be 8.5 wt% when moisture sorption/desorption equilibrium was reached under 90% RH and at 25°C.[77] Notably, M2 afforded a swelling ratio as high as ~21.4 g g^{-1} across a broad LiCl concentration range (20 − 40 wt%). In this case, the capability of salt solution retention of swelled M2 was significantly higher than the overall mass of hydrated M2 at equilibrium, indicating effective prevention of LiCl solution leakage.

A cyclic moisture sorption−desorption experiment was performed to evaluate the stability of M3 (**Figure 3i**). Under 90% RH and at 25 °C, the M3 sample (size: 15× 15 × 3 mm^3) achieved water uptake of 175.6 g m^{-2} in the first 9 h. Water desorption was subsequently performed by heating the M3 sample on a hot plate at 55 °C, leading to water release of 213.8 g m^{-2} after 3 h. Remarkably, no discernible degradation in water uptake or release capacity was observed over 20 sorption−desorption cycles. M3 exhibited swelling during moisture sorption while maintaining its structural integrity during water desorption, with negligible structural collapse. The morphologies of the dual layers within M3 before and after the sorption−desorption cycles were characterized. Scanning electron microscope (SEM) images confirmed that the solid

structure of the cross-sections in both M1 and M2 layers remained intact (Figure S21, Supporting Information). Elemental mapping via SEM with energy-dispersive X-Ray spectrometry (EDS) reveals that C, O, N, S and Cl were evenly distributed throughout initial M3 structure. A distinct interface between M1 and M2 was evident, characterized by the higher concentrations of C, O, N and S in M2, while M1 exhibited an elevated Cl content. These variations in EDS mapping are in good agreement with the distinct material compositions (i.e., DMAPS and LiCl contents) within M1 and M2. After 20 sorption−desorption cycles, both layers retained their original elemental distributions and compositions. Notably, no anisotropic enrichment of Cl was observed in either layer. These results demonstrate minimized LiCl leakage away from M3.

2.3 Passive Cooling Characterization of M3-Covered Solar Cells

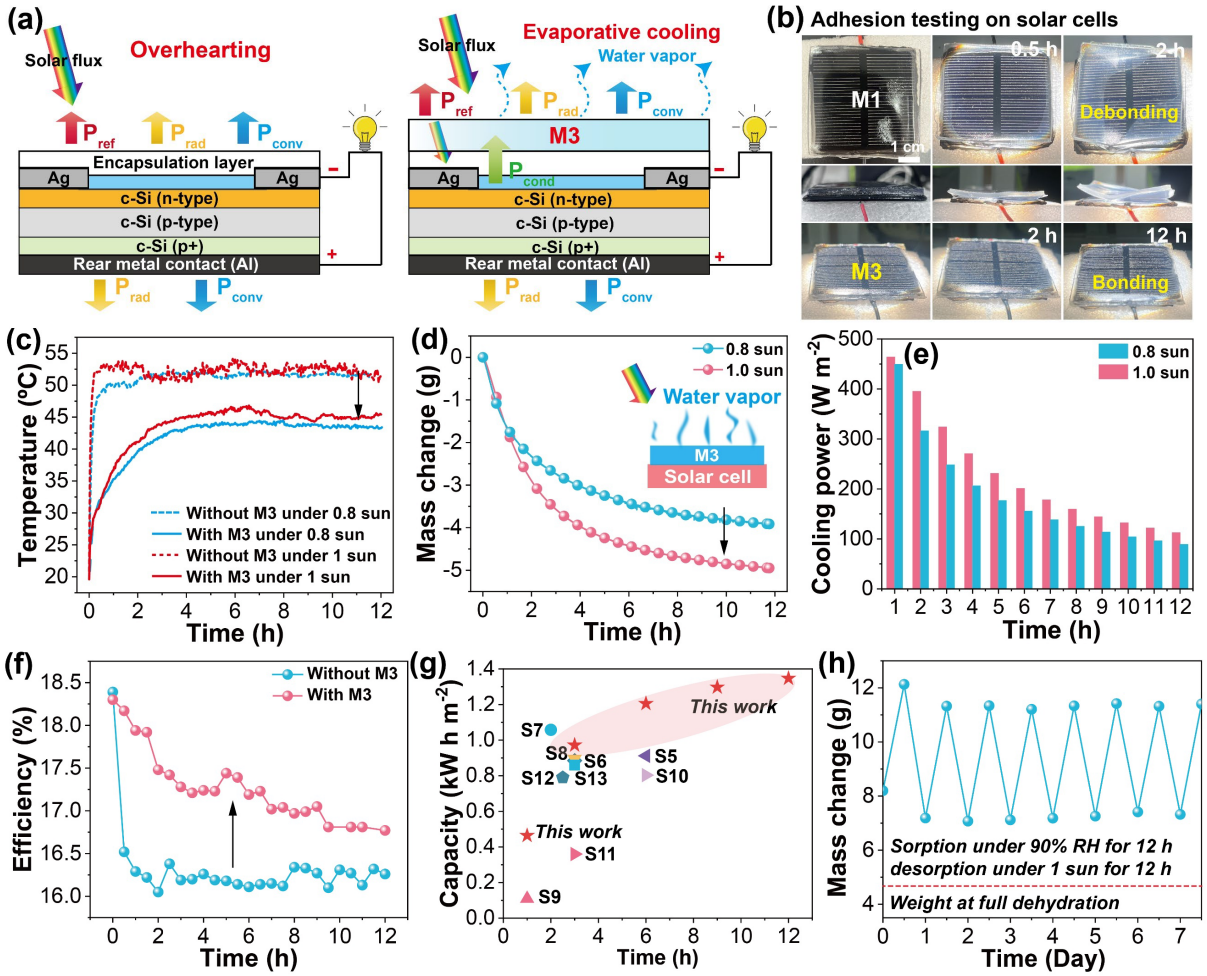

Figure 4. (a) Schematic illustration of solar panels without and with M3 on top. (b) Adhesion

testing of M1 and M3 under solar irradiation over time. (c) Surface temperature variations of solar panels under solar irradiation over 12 h. (d) Mass changes and (e) cooling power of M3 under solar irradiation over 12 h. (f) PCE variations of solar panels without and with M3 over 12 h. (g) Summary of passive cooling power of recent hygroscopic materials used for solar cells. (h) Mass changes of the M3-covered solar cell in moisture sorption−desorption cycles.

In conventional *c*-Si solar cells, a portion of the incident photons that is not converted into electricity is dissipated as optical loss (reflection) and waste heat. The heat loss is primarily released through convection and radiation into the surrounding environment (**Figure 4a**). Without additional cooling methods, air-driven passive cooling pathways are inefficient, resulting in significant "overheating" of conventional solar panels — temperatures can rise by up to 70 °C under real-world conditions.[81] Such thermal stress not only reduces power conversion efficiencies (PCEs) but also shortens the operational lifespan of solar cells.[9] To address this issue, M3 was integrated onto the surface of the *c*-Si solar cells to boost photovoltaic performance through passive cooling (Video S3, Supporting Information). Indoor experiments were conducted to measure surface temperatures, mass changes, photovoltaic parameters, cooling performance and durability of M3-covered *c*-Si solar panels. First, *c*-Si solar cells integrated with M1 or M3 (size: 50 × 50 × 3 mm^3) were subjected to continuous exposure under 1 sun (1000 W m^{-2}, AM1.5) (**Figure 4b**). Owing to the negligible adhesion strength of M1, significant edge warping occurred during solar-driven dehydration after 2 h. In contrast, no deformation or edge warping was observed in M3 even after 12 h of solar irradiation, due to its high adhesion strength on the glass substrate. This result highlights the dual-layer design of M3, which featured a robust bonding layer that adhered firmly to the solar cell surface, ensuring a durable interface for passive cooling and conduction.

Surface temperatures of *c*-Si solar cells without and with M3 were evaluated over time under the same conditions (~20 °C and ~50% RH). Considering the daylight duration, all solar cells were subjected to uniform and continuous irradiation with simulated sunlight (0.8 or 1.0 sun)

for 12 h. Within 0.5 h, surface temperatures of the conventional solar cells rapidly increased to 48.9 and 53.1 °C under 0.8 and 1 sun, respectively (**Figure 4c** and Figure S22, Supporting Information). These elevated temperatures persisted for over 12 h of continuous solar irradiation, indicating significant heat losses and overheating of these solar cells. On the other hand, the M3-covered solar panels exhibited a more gradual temperature increase over time under both 0.8 and 1.0 sun. Under 0.8 sun, the surface temperature of the M3-integrated solar cell reached 43.4 °C after 12 h, leading to a temperature reduction of 8.9 °C compared to the conventional solar cell. Under 1.0 sun, the surface temperature of the M3-integrated solar cell reached 45.5 °C after 12 h, yielding a 7.7 °C temperature reduction compared to the conventional solar cell. In addition, the weight loss profiles of M3 were used to quantify heat-driven water evaporation over 12 h (**Figure 4d**). On top of the solar panels, M3 exhibited a water loss of 32.2% and 40.5% of water after 12 h under 0.8 and 1.0 sun, respectively. Associated with the heat-induced water loss, the evaporation cooling power (P_{ec}) delivered by M3 to the solar panel over time can be calculated using equation 1,[45]

$$P_{ec} = \frac{\Delta H_{vap} \times \Delta m}{t \times A} \qquad (1)$$

where $\triangle H_{vap}$ represents the enthalpy of vaporization of water (~2450 J g^{-1}), $\triangle m$ denotes the weight loss of M3 due to water evaporation, t is the test duration and A is the surface area of M3 (50 × 50 mm^2) applied onto the solar cell. The average P_{ec} values of M3 over 12 h of solar irradiation are summarized in **Figure 4e**. Under 0.8 sun, the average P_{ec} values were 449.3, 248.0, 155.6 and 89.1 W m^{-2} within 1, 3, 6 and 12 h, respectively. As water evaporated, the LiCl solutions within M3 underwent continuous concentration, leading to a progressive decline in evaporation rates and average cooling power. Under 1.0 sun, the average P_{ec} values were 463.8, 323.8, 200.8 and 112.2 W m^{-2} within 1, 3, 6 and 12 h, respectively. Increased solar intensity resulted in elevated surface temperatures of the solar panel, which synergistically enhanced both water evaporation and the cooling performance of M3. Since the negligible

contribution of radiation cooling under indoor conditions, these results highlight the effectiveness of M3 in reducing and maintaining lower surface temperatures of solar panels through evaporative cooling.

Photovoltaic performance of *c*-Si solar cells without and with M3 was evaluated over time under the same conditions (1.0 sun, ~20 °C and ~50% RH). The current−voltage (*J*−*V*) curves of solar cells were plotted in Figure S23, Supporting Information. Main photovoltaic parameters including open-circuit voltage (V_{oc}), short-circuit current (J_{sc}), fill factor (FF), maximum power output (P_{max}) and PCEs were derived from *J*−*V* curves and are summarized in Table S3 and S4, Supporting Information. Under 1.0 sun, the conventional *c*-Si solar cell (active area: 50 × 50 mm^2) initially afforded a V_{oc} of 2.607 V, a J_{sc} of 8.5 mA cm^{-2} and a FF of 0.83, leading to a high PCE of 18.39%. As the surface temperature gradually increased, the gradual decreases in V_{oc} and FF, coupled with a steady J_{sc}, led to a notable decline in PCE to 16.26% after 12 h, respectively (**Figure 4f**). On the other hand, the integration of M3 (size: 50 × 50 × 3 mm^3) atop the solar cell initially achieved a V_{oc} of 2.629 V, a J_{sc} of 8.7 mA cm^{-2} and a FF of 0.80, yielding a high PCE of 18.30%. This result confirms that the incorporation of this thin, transparent membrane did not significantly compromise the initial photovoltaic performance of the conventional solar cell, which is in good agreement with its high transmittance across the wavelength range of 270 − 1450 nm. In addition, the M3-covered solar cell effectively mitigated overheating, preventing rapid degradation of key photovoltaic parameters including V_{oc}, FF and PCEs over time. During 12 h of continuous illumination under 1 sun, both PCEs and P_{max} of the M3-covered solar cell consistently outperformed the conventional solar cell (Figure 4f and Figure S24, Supporting Information). Specifically, the M3-covered solar cell achieved an average PCE improvement (△PCE) of 1.0%, with a peak △PCE of 1.7%. Compared to recently reported hygroscopic hydrogels and coatings for solar cell cooling, M3 demonstrates superior performance in both evaporative cooling power and sustained cooling duration, as summarized

in **Figure 4g** and Table S5, Supporting Information. These results highlight the exceptional evaporative cooling capabilities of M3, offering an exciting solution for mitigating overheating and boosting photovoltaic performance of solar cells through a top-covered, direct-contact design. In addition, main parameters including transmittance, emittance, water uptake, solar temperature reduction and solar efficiency enhancement of various passive cooling materials and methods for solar cells are summarized in Table S6, Supporting Information. The corresponding radar plot presented in the Table of Contents graphic illustrates the advantages of the spectrally-tailored hygroscopic hydrogels with Janus interfaces and enhanced hybrid passive cooling for solar cells developed in this study.

A cyclic moisture sorption−desorption experiment, along with photovoltaic, water content and transmittance characterization, was performed on the M3-coated solar cell (**Figure 4h**). The experiment simulated natural diurnal cycles by alternating 12 h periods of water vapor sorption at night with 12 h periods of desorption during the daytime, and continued for 7 days. When subjected to 90% RH and 25°C, as-prepared M3 (50 × 50 × 3 mm^3, 8.2 g) absorbed 3.9 g of water from air over 12 h. Following the desorption process under 1 sun, M3 lost 4.9 g of water over subsequent 12 h. Notably, no edge warping or detachment of M3 from the solar panel was observed, and its moisture absorption and desorption capabilities remained stable over multiple cycles. After 12 h of solar-driven desorption, the mass of M3 (7.2 g) remained higher than its fully dehydrated weight (4.8 g). Even after 48 h of continuous 1 sun irradiation, M3 did not reach complete dehydration, retaining a mass of 6.3 g, which corresponded to ~53% of the water content relative to its initial state (Figure S25a, Supporting Information). Compared to the conventional solar cell (PCE = 16.25%), the M3-covered solar cell retained a higher PCE of 16.55% after 48 h, indicating its sustained evaporative cooling performance under prolonged solar irradiation (Figure S25b, Supporting Information). Moreover, the image sequence presents that M3 can retain high transparency for up to 48 h during continuous solar irradiation

and water desorption (Figure S26, Supporting Information). Its average transmittance in the 450 − 950 nm range did not rapidly decline under solar-driven dehydration, due to its high water retention. Notably, M3 preserved 82.5% of its water content and ~90% average transmittance (450 − 950 nm) throughout a full day (up to 12 h) of solar irradiation (Figure S27, Supporting Information). Even after 48 h of continuous 1 sun exposure, M3 retained ~83% of its initial transmittance. This sustained optical clarity stemmed from high bound/intermediate water contents stabilized by LiCl complexes and zwitterionic networks. These results highlight the stable optical properties, reliable sorption−desorption cycling and stable cooling performance of M3-covered solar cells for boosting green electricity generation.

2.4 Outdoor Experiments on Hybrid Passive Cooling

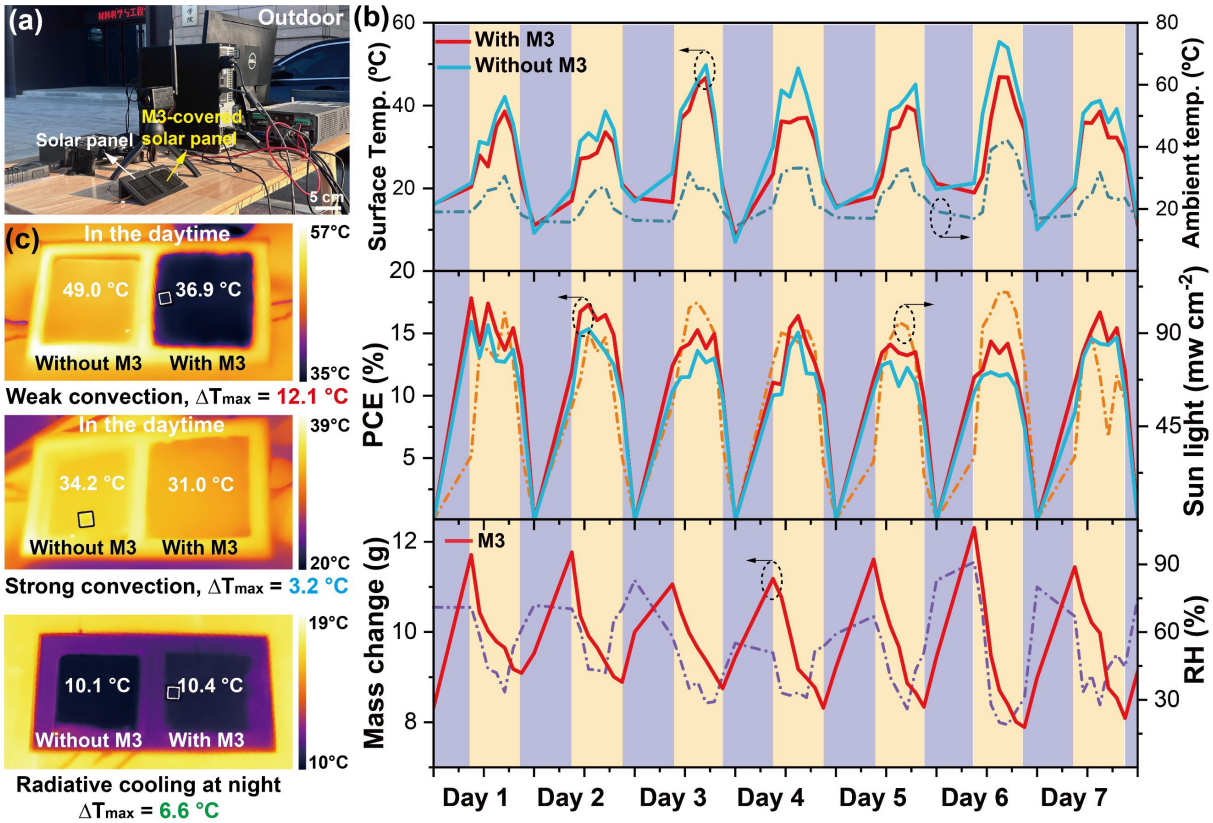

Figure 5. Outdoor experiments: (a) Experimental setup of passive cooling tests for *c*-Si solar cells in outdoor conditions. (b) Summary of main parameters of solar cells and environment over 7 days' outdoor measurements. (c) IR images of solar panels in different weather conditions.

Outdoor experiments were conducted in May, Qingdao, China, to evaluate the passive cooling performance of M3-coated solar cells under real sky. Both *c*-Si solar cells with and without M3 cover were mounted in a 3D-printed plastic scaffold, inclined at 30° relative to the horizontal plane (**Figure 5a**). To ensure a reliable comparison, both *c*-Si solar cells featured an identical active area of 50 × 50 mm^2 and afforded comparable initial performance. The variations in surface temperatures, M3's weights, photovoltaic performance and main environmental parameters (i.e., solar intensity, ambient temperature and RH) were recorded at regular intervals over 7 days, with all data summarized in **Figure 5b**. During early summer, solar intensity ranged from 20 − 110 mW cm^{-2} in the daytime under real sky. Notably, the surface temperatures and PCEs of the solar cells fluctuated in response to variations in solar intensity. The highest surface temperatures and PCEs were generally observed at noon, when solar intensity was maximal. The M3-covered solar cell exhibited a significant reduction in the surface temperatures compared to the conventional solar cell throughout the day, indicating its effective passive cooling performance. Specifically, the temperature difference reached a peak of 12.1 °C on a sunny day with negligible air convection (Day 4, air velocity: 0.2 m s^{-1}). A moderate temperature difference of 3.2 °C was retained when significant convection was present (Day 3, air velocity: 4.0 m s^{-1}).

During the daytime, RH values remained relatively low, ranging from 19% to 71%. Under these conditions, M3 on the solar cell exhibited continuous weight loss due to solar-driven evaporation. On the other hand, RH values significantly increased at night, ranging from 70% to 91%. High RH values facilitated water vapor sorption and weight gain (regeneration) of partially dehydrated M3. This alternating cycle of water vapor sorption and desorption followed a distinct zigzag pattern between night and day, indicating the rapid responsiveness and high stability of M3 to diurnal RH fluctuations. At a clear night (Night 6, air velocity: 1.0 m s^{-1}), the night-time radiative cooling effect of the conventional *c*-Si solar panel reduced its surface

temperature below the ambient temperature, due to its naturally high emissivity in MIR wavelength range. Notably, the surface temperatures of the M3-covered solar cell were ~6 °C lower than the ambient temperature. This observation serves as additional evidence for the radiative cooling effect induced by M3 on solar panels. This radiative cooling effect counteracted the exothermic heat generated by water vapor sorption of M3, effectively reducing the surface temperature of the M3-covered solar panel. Consequently, this temperature decreases facilitated atmospheric water sorption and regeneration of M3 by increasing effective RH and P_{vapor} difference. These results highlight the synergistic effects of evaporative and radiative cooling in the M3-covered solar cell.

Leveraging the combined passive cooling effects, the M3-covered solar cell attained superior PCEs over 7 days' measurements, outperforming the conventional solar cell. The PCE differences were most pronounced around noon, exhibiting an average PCE improvement of 2.6% over 7 days. Notably, the passive cooling effects and PCE enhancements were influenced by the RH values from the preceding night, and main environmental factors (i.e., solar intensity and airflow) on the following day. Specifically, when RH was high during the previous night, and solar intensity was strong with weak airflow the next day, the passive cooling performance of M3 was maximized, yielding 21.3% PCE improvement (△PCE = 2.9%) at noon (Figure S28, Supporting Information).

In addition to the indoor experiments on performance stability and LiCl leakage, outdoor tests were conducted to further validate the reliability of the integrated device. A M3-covered solar cell was exposed to outdoor conditions for 15 days. The image sequence reveals no visible LiCl residues on either the surface or edges of the solar cell (Figure S29, Supporting Information). Importantly, the back circuit remained uncorroded, indicating no LiCl solution leakage. The zwitterionic polymer-mediated anti-polyelectrolyte effect, combined with the large-volume swelling behavior of M3, synergistically enhanced the retention of LiCl and its solution,

effectively mitigating LiCl leakage from M3. Furthermore, the image sequence exhibits that the M3 layer retained high optical clarity and displayed no obvious signs of UV-induced yellowing after 15 days of outdoor exposure (Figure S30, Supporting Information). These preliminary results disclose the efficiency and reliability of the hybrid passive cooling mechanism in M3, highlighting its great potential to boost photovoltaic performance of solar panels under real-sky conditions.

Dust contamination is another major operational challenge for solar cells, especially in arid and industrial areas. Dust accumulation reduces power output, causes uneven energy generation, and accelerates surface corrosion. Consequently, regular cleaning — whether manual, robotic, or automated — is essential to maintain energy yield and extend panel lifespan.[82] To evaluate cleanability, a conventional *c*-Si solar cell and an M3-covered *c*-Si solar cell were exposed to dust-laden environments for 48 h. Dust on both surfaces was easily removed by wiping with a damp cloth (Figure S31, Supporting Information). The manual cleaning process for the M3-covered solar cell is demonstrated in Video S4, Supporting Information. This result indicates the cleanable surface property of the M3-covered solar cells, attributed to the Janus-like adhesion design.

2.5 Applicability Characterization in Organic Flexible Photovoltaics

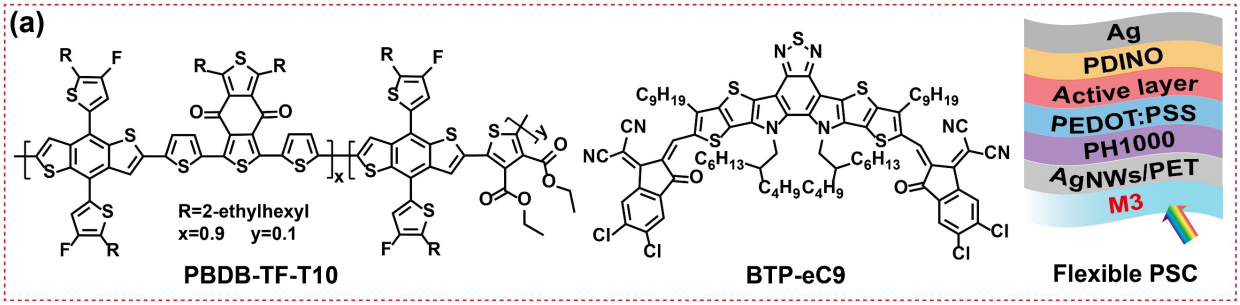

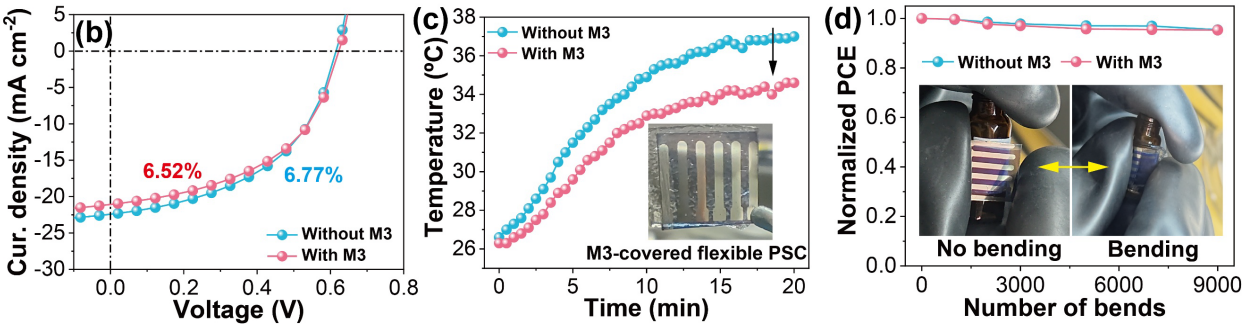

Figure 6. Applicability characterization: (a) Chemical structures of main light-absorbing materials and device configuration of flexible PSCs. (b) Initial *J*–*V* curves of flexible PSCs without and with M3 under 1 sun. (c) Surface temperature changes of flexible PSCs without and with M3 under 1 sun over time (the inset image shows a digital photograph of flexible PSC integrated with M3 on top). (d) Normalized PCEs of flexible PSCs without and with M3 after 10000 bending cycles at a bending radius of 5 mm (inset images show the bending test).

Polymer solar cells (PSCs), as one of the most enduring alternatives to *c*-Si solar cells, offer distinct advantages, including enhanced transparency, flexibility, integrability and aesthetic appeal.[83] Recent development of non-fullerene electron-acceptors and ternary strategies have substantially improved PCEs and operational lifetime of PSCs.[84] Given that M3 demonstrates Janus adhesion, exceptional transparency, high flexibility and mechanical robustness, a 1-mm layer of M3 was applied to flexible PSCs to broaden their applicability in this emerging photovoltaic technology. Integration of M3 onto flexible PSCs offers significant potential for scaling up power generation in wearable and portable electronics, facilitated by passive thermal management.[85]

Chemical structures of the main light-absorbing materials and the device configuration for the fabrication of flexible PSCs are depicted in **Figure 6a**. A terpolymer (named PBDB-TF-T10) was employed as the electron donor, while small molecule BTP-eC9, a representative non-fullerene electron acceptor, was combined with the fullerene acceptor $PC_{71}BM$, forming ternary PSCs.[86] The absorptance spectra and absorption coefficients of these materials were measured and are presented in Figure S32, Supporting Information. The absorbance spectrum of PBDB-

TF-T10 in its film state ranged from 350 to 700 nm, exhibiting a maximum absorption coefficient of ~6.7×10^4 cm^{-1} at 560 nm. For BTP-eC9, its film absorption spectrum spanned 429 to 1000 nm, with the highest absorption coefficient of ~11.1×10^4 cm^{-1} at 826 nm. The complementary absorption profiles of PBDB-TF-T10, BTP-eC9 and $PC_{71}BM$ afforded broad absorption band (350 − 1000 nm), covering the entire visible range and extending into NIR region. In addition, flexible PSCs were fabricated using the device configuration of polyethylene terephthalate (PET)/silver nanowires (AgNWs)/PH1000 (160 nm)/PEDOT:PSS (20 nm)/active layer (100 nm)/PDINO (5 nm)/Ag (80 nm). The intrinsic flexibility of polymer materials and flexible electrodes conferred enhanced durability to PSCs, enabling effective deformation without compromising performance.[86]

Passive cooling and photovoltaic performance of PSCs were evaluated under 1 sun. Owing to the high transmittance of M3 in the wavelength range of 270 − 1450 nm, the *J*–*V* curves show that M3-covered flexible PSC afforded a high PCE of 6.52%, closely approaching PCE of the control device (6.77%) (**Figure 6b**). For flexible PSC without M3, the surface temperature significantly increased from 26.6 to 37.0 °C after 20 min of solar irradiation (**Figure 6c**). In contrast, the M3-covered flexible PSC effectively mitigated this temperature rise, reaching only 34.6 °C after 20 min. Corresponding *J*–*V* curves and photovoltaic parameters are summarized in Figure S33 and Table S7, Supporting Information. Without using M3, flexible PSC experienced a clear PCE decrease from 6.54% to 6.18% after 20 min of exposure to 1-sun irradiation. On the other hand, the M3-covered device retained ~98% of its initial PCE (6.65%) over the same period. These results reveal that the evaporative cooling effect induced by M3 can enhance the performance stability of flexible PSCs.

A bending test was performed to assess the durability of M3-covered flexible PSCs against repeated deformation. The *J*–*V* curves of flexible PSCs without and with M3 were measured during 10000 bending cycles with a bending radius of 5.0 mm (**Figure 6d** and Figure S34,

Table S8 and S9, Supporting Information). Remarkably, both devices retained ~95% of their initial PCEs after 10000 continuous bending cycles, placing their mechanical endurance among the top-performing flexible PSCs reported to date.[87] Notably, no slippage or debonding occurred between M3 and underlying PSC (Video S5, Supporting Information). Moreover, the surface temperature of flexible PSC remained stable during the entire bending test, indicating negligible heat generation due to mechanical deformation (Figure S35, Supporting Information). These results highlight the exceptional robustness of M3-covered PSCs in withstanding external mechanical stress while retaining high efficiency for foldable photovoltaic applications.

3. Conclusions

In summary, hygroscopic hydrogel membranes were successfully fabricated as transparent surface plates through the synergistic engineering of polymer components, cross-linking networks, LiCl contents, two-layered structures and surface asymmetry. This design combined selected optical windows, moisture sorption/desorption, hybrid passive cooling and solar power enhancement when applied to the front surfaces of both *c*-Si (inorganic) and flexible (organic) solar cells. The main advantages of our design are summarized as follows (i−iv): i) Hygroscopic LiCl-embedded hydrogels with both highly cross-linked and highly entangled networks were integrated into M3. This dual-layered structure with controlled thickness (3 mm) ensured high transparency, structural integrity, mechanical robustness and durability. ii) The distinct cross-linking strategies with varying polymer and LiCl contents enabled efficient water vapor sorption and LiCl solution absorption in both layers, while inducing the directional water diffusion and adhesive−antiadhesive surfaces for sub-layers (M1 and M2) of M3. The salt-in effect from highly concentrated zwitterionic copolymers and large-volume swelling stabilized the highly concentrated LiCl solutions (10 and 20 wt%) in both layers without leakage. iii) The water uptake of M3 significantly exceeded that of M1 or M2 alone, reaching 282.22 g m^{-2} under 90% RH after 24 h. Rapid water release occurred across a broad temperature range (45 − 65 °C).

This reliable moisture sorption/desorption resulted in effective evaporative cooling for solar panels during day−night transitions. Furthermore, M3 provided high transmittance (~90.0%) in the absorption bands (300 − 1100 nm) of *c*-Si solar cells, and achieved high emissivity (~98.1%) in the MIR wavelength range for sky radiative cooling. As a result, the M3-covered *c*-Si solar cells achieved a maximized temperature decrease by ~12 °C, leading to a 21.3% increase in PCE under natural sunlight. Nighttime radiative cooling reduced the panel temperature by ~6 °C, facilitating cooling power regeneration overnight. Additionally, this membrane demonstrated excellent passive cooling, flexibility and integration in emerging flexible solar cells, retaining ~95% of PCE over 10000 bending cycles. These self-contained functions and hybrid cooling mechanisms distinguish M3 from a variety of passive cooling materials used for solar panels and other electronics. This work paves intriguing prospects for developing hierarchically aligned hydrogels for hybrid passive cooling, not only scaling up solar energy generation for solar panels, but also considering transparency, surface asymmetry, flexibility and integrability for energy-wise thermal management of diverse electronic devices.

4. Experimental Section

4.1 Material Preparetion

Preparation of M1: DMAPS powder (14.2 wt%), PAC powder (1 wt%), HEEA solution (5.8 wt%), LiCl, and the cross-linking agent PEGDA (1 wt% of the total DMAPS and HEAA content), along with an equal mass to the crosslinking agent *α*-ketoglutaric acid (*α*-T), were dissolved in deionized water and thoroughly stirred to form a transparent solution. Subsequently, the precursor solution is poured into a mold and subjected to UV-assisted polymerization in a UV chamber (18 W and 365 nm) for 10 min, yielding a transparent M1 film.

Preparation of M2: DMAPS powder, HEEA solution, LiCl, and the cross-linking agent N,N'-methylenebisacrylamide (MBA), along with *α*-T, were dissolved in water and thoroughly stirred to form a transparent solution (details in Table S1, Supporting Information). Specifically,

the molar ratio of the crosslinking agent to the total monomer content was fixed at 1.0×10^{-5}, and the molar ratio of the initiator to the crosslinking agent was 2:5. The precursor solution was then poured into a mold, UV-assisted polymerization was performed in an UV chamber (18 W and 365 nm) for 10 min, yielding a transparent M2 film.

Preparation of M3: After adding a certain amount of M1 precursor solution into a mold and conducting UV-assisted polymerization for 10 min, an equivalent volume of M2 precursor solution was poured into the mold and subjected to UV-assisted polymerization for another 10 min. This layer-by-layer fabrication results in a transparent M3 film.

4.2 Water vapor sorption and desorption

Water vapor sorption was evaluated in an artificial climate chamber (RGC-160D, Youke) at controlled temperatures and RHs. Solar-powered dehydration was conducted at ~25 °C and ~50% RH using a xenon lamp (CEL-S500, CEAULIGHT) with an AM 1.5G optical filter. Calibration of the solar flux was achieved through a thermopile connected to a power meter (CEL-NP2000, CEAULIGHT). Thermal dehydration was conducted using a natural convection oven. Mass changes of water were continuously monitored in real-time using a high-precision electronic balance (QUINTIX224-1CN, Sartorius, accuracy: 0.1 mg). Outdoor experiments were conducted during May in Qingdao, China. Temperature distribution was monitored by an IR camera (223s-L19, Fotric Precision Instruments) and thermocouples.

4.3 Preparation of flexible PSCs

Flexible PSCs were fabricated in a glovebox with temperature: 20 °C, oxygen: 0.1 ppm and water: 0.1 ppm. First, the PET/AgNWs substrates were gently scrubbed with a cotton dipping ethanol. Then, PEDOT:PSS (PH1000) aqueous with 5 wt% ethylene glycol and 1.5 vol.% FS3000 was spin-coated with 1500 rpm for 60 s on top of PET/AgNWs substrates filtered with 0.45 μm syringe filter, followed by thermal annealing at 100 °C for 15 min. The PEDOT:PSS layer was then prepared by spin-coating at 3000 rpm for 30 s and annealed at 150 °C for 15

min. After that, the active layer was spin-coated onto the PEDOT:PSS layer at 4000 rpm for 35 s followed by annealing at 110 °C for 10 min. A PDINO layer (1 mg mL^{-1} in methanol) was spin-coated onto the active layer at 3000 rpm for 25 s. Finally, Ag was deposited through shadow masks (0.07 cm^2) by thermal evaporation under 4×10^{-4} Pa. The thicknesses of thin films were measured by a contact profilometer (Dektak XT, Bruker).

Declaration of competing interest

The authors declare no conflict of interest.

Acknowledgements

The authors acknowledge the financial support from the National Natural Science Foundation of China (Grant No. 22379133 and 22179040), the Fundamental Research Funds for the Central Universities, China (Grant No. 842461106), the Taishan Scholar Program of Shandong Province, China (Grant No. tsqn201812026), the Natural Science Foundation of Shandong Province, China (Grant No. ZR2023MB087), and the Natural Science Foundation of Qingdao, China (Grant No. 23-2-1-243-zyyd-jch).

References

[1] N. M. Haegel, H. Atwater, T. Barnes, C. Breyer, A. Burrell, Y.-M. Chiang, S. De Wolf, B. Dimmler, D. Feldman, S. Glunz, J. C. Goldschmidt, D. Hochschild, R. Inzunza, I. Kaizuka, B. Kroposki, S. Kurtz, S. Leu, R. Margolis, K. Matsubara, A. Metz, W. K. Metzger, M. Morjaria, S. Niki, S. Nowak, I. M. Peters, S. Philipps, T. Reindl, A. Richter, D. Rose, K. Sakurai, R. Schlatmann, M. Shikano, W. Sinke, R. Sinton, B. J. Stanbery, M. Topic, W. Tumas, Y. Ueda, J. van de Lagemaat, P. Verlinden, M. Vetter, E. Warren, M. Werner, M. Yamaguchi, A. W. Bett, *Science* **2019**, 364, 836.

[2] T. Liu, M. M. S. Almutairi, J. Ma, A. Stewart, Z. Xing, M. Liu, B. Hou, Y. Cho, *Nanomicro Lett.* **2024**, 17, 49.

[3] K. J. Prince, H. M. Mirletz, E. A. Gaulding, L. M. Wheeler, R. A. Kerner, X. Zheng, L. T. Schelhas, P. Tracy, C. A. Wolden, J. J. Berry, S. Ovaitt, T. M. Barnes, J. M. Luther, *Nat. Mater.* **2025**, 24, 22.

[4] B. Liang, X. Chen, X. Wang, H. Yuan, A. Sun, Z. Wang, L. Hu, G. Hou, Y. Zhao, X. Zhang, *J. Mater. Chem. A* **2025**, 13, 2441.

[5] J. Zhu, J. Xia, Y. Li, Y. Li, *ACS Appl. Mater. Interfaces* **2025**, 17, 5595.

[6] L. C. Hirst, N. J. Ekins-Daukes, *Prog. Photovolt: Res. Appl.* **2011**, 19, 286.

[7] Z. Shao, P. Poredoš, R. Wang, *Joule* **2024**, 8, 280.

[8] O. Bamisile, C. Acen, D. Cai, Q. Huang, I. Staffell, *Renew. Sustain. Energy Rev.* **2025**, 208, 115073.

[9] L. Xu, W. Liu, H. Liu, C. Ke, M. Wang, C. Zhang, E. Aydin, M. Al-Aswad, K. Kotsovos, I. Gereige, A. Al-Saggaf, A. Jamal, X. Yang, P. Wang, F. Laquai, T. G. Allen, S. De Wolf, *Joule* **2021**, 5, 631.
[10] B. Wei, W. Luo, J. Du, Y. Ding, Y. Guo, G. Zhu, Y. Zhu, B. Li, *SusMat* **2024**, 4, e239.
[11] H. Liu, C. Yang, R. Wang, *Device* **2025**, 3, 100684.
[12] N. Zhang, T. Jiang, C. Guo, L. Qiao, Q. Ji, L. Yin, L. Yu, P. Murto, X. Xu, *Nano Energy* **2020**, 77, 105111.
[13] F. Wang, N. Xu, W. Zhao, L. Zhou, P. Zhu, X. Wang, B. Zhu, J. Zhu, *Joule* **2021**, 5, 1602.
[14] Q. Ji, N. Li, S. Wang, S. Li, F. Li, L. Yu, P. Murto, X. Xu, *J. Mater. Chem. A* **2021**, 9, 21197.
[15] F. Li, Y. Sui, H. Lin, Z. Sui, K. Lee, S. Xie, W. Zeng, Z. Ding, H.-L. Yip, W. Wu, *Device* **2025**, 3, 100569.
[16] Q. Zhang, Y. Li, C. Liu, X. Wu, X. Zhang, J. Song, Y. Mao, K. Yuan, *J. Mater. Chem. A* **2024**, 12, 32526.
[17] Z. Wang, H. Hölzel, L. Fernandez, A. S. Aslam, P. Baronas, J. Orrego-Hernández, S. Ghasemi, M. Campoy-Quiles, K. Moth-Poulsen, *Joule* **2024**, 8, 2607.
[18] J. Wei, H. Chen, J. Liu, F. Wang, C. Wang, *Nano Energy* **2025**, 136, 110680.
[19] C. D. Díaz-Marín, L. Zhang, B. E. Fil, Z. Lu, M. Alshrah, J. C. Grossman, E. N. Wang, *Int. J. Heat Mass Transfer* **2022**, 195, 123103.
[20] J. Li, X. Wang, D. Liang, N. Xu, B. Zhu, W. Li, P. Yao, Y. Jiang, X. Min, Z. Huang, S. Zhu, S. Fan, J. Zhu, *Sci. Adv.* **2022**, 8, eabq0411.
[21] Z. Lu, E. Strobach, N. Chen, N. Ferralis, J. C. Grossman, *Joule* **2020**, 4, 2693.
[22] D. F. Hanks, Z. Lu, J. Sircar, I. Kinefuchi, K. R. Bagnall, T. R. Salamon, D. S. Antao, B. Barabadi, E. N. Wang, *ACS Appl. Mater. Interfaces* **2020**, 12, 7232.
[23] Z. Xu, L. Zhang, L. Zhao, B. Li, B. Bhatia, C. Wang, K. L. Wilke, Y. Song, O. Labban, J. H. Lienhard, R. Wang, E. N. Wang, *Energy Environ. Sci.* **2020**, 13, 830.
[24] W. Wang, Y. Shi, C. Zhang, R. Li, M. Wu, S. Zhuo, S. Aleid, P. Wang, *Nano Lett.* **2021**, 21, 5068.
[25] Y. Shao, A. Shen, N. Li, L. Yang, J. Tang, H. Zhi, D. Wang, G. Xue, *ACS Appl. Mater. Interfaces* **2022**, 14, 30324.
[26] D. Zhang, Y. Wan, W. Zhuang, X. Geng, P. Yang, *Chem. Eng. J.* **2023**, 466, 143047.
[27] Z. Zhu, H. Zheng, H. Kong, X. Ma, J. Xiong, *Nat. Water* **2023**, 1, 790.
[28] Z. Xu, J. Yu, H. Shan, J. Wang, J. Gao, Z. Ye, R. Wang, *Energy Environ. Sci.* **2023**, 16, 5325.
[29] J. Gao, L. Zhang, J. You, Z. Ye, Y. Zhong, R. Wang, E. N. Wang, Z. Xu, *Joule* **2023**, 7, 2274.
[30] M. Liu, Y. Sun, K. Shao, N. Li, J. Li, P. Murto, Z. Wang, J. Chen, X. Xu, *Nano Energy* **2024**, 119, 109074.
[31] J. Xu, P. Wang, Z. Bai, H. Cheng, R. Wang, L. Qu, T. Li, *Nat. Rev. Mater.* **2024**, 9, 722.
[32] R. Li, P. Wang, *Nat. Water* **2023**, 1, 573.
[33] S. Guo, Y. Zhang, S. C. Tan, *Device* **2023**, 1, 100099.
[34] Y. Zhong, L. Zhang, X. Li, B. El Fil, C. D. Díaz-Marín, A. C. Li, X. Liu, A. LaPotin, E. N. Wang, *Nat. Rev. Mater.* **2024**, 9, 681.
[35] W. Zeng, T. You, W. Wu, *Nano Energy* **2024**, 125, 109572.
[36] C. Lei, W. Guan, Y. Zhao, G. Yu, *Chem. Soc. Rev.* **2024**, 53, 7328.
[37] S. Bai, X. Yao, M. Y. Wong, Q. Xu, H. Li, K. Lin, Y. Zhou, T. C. Ho, A. Pan, J. Chen, Y. Zhu, S. Wang, C. Y. Tso, *ACS Nano* **2024**, 18, 31597.
[38] Y. Song, M. Zeng, X. Wang, P. Shi, M. Fei, J. Zhu, *Adv. Mater.* **2024**, 36, 2209134.
[39] Q. Li, F. Wang, Y. Zhang, M. Shi, Y. Zhang, H. Yu, S. Liu, J. Li, S. C. Tan, W. Chen,

Adv. Mater. **2024**, 36, 2209479.
[40] S. Guo, S. C. Tan, *Joule* **2024**, 8, 291.
[41] C. Wang, L. Hua, H. Yan, B. Li, Y. Tu, R. Wang, *Joule* **2020**, 4, 435.
[42] Y. Hu, W. Yang, W. Wei, Z. Sun, B. Wu, K. Li, Y. Li, Q. Zhang, R. Xiao, C. Hou, H. Wang, *Sci. Adv.* 10, eadk4620.
[43] K. Yang, T. Pan, N. Ferhat, A. I. Felix, R. E. Waller, P.-Y. Hong, J. S. Vrouwenvelder, Q. Gan, Y. Han, *Nat. Commun.* **2024**, 15, 6260.
[44] S. Pu, J. Fu, Y. Liao, L. Ge, Y. Zhou, S. Zhang, S. Zhao, X. Liu, X. Hu, K. Liu, J. Chen, *Adv. Mater.* **2020**, 32, 1907307.
[45] R. Li, Y. Shi, M. Wu, S. Hong, P. Wang, *Nat. Sustain.* **2020**, 3, 636.
[46] E. Gkaniatsou, B. Meng, F. Cui, R. Loonen, F. Nouar, C. Serre, J. Hensen, *Nano Energy* **2021**, 87, 106224.
[47] R. Li, M. Wu, S. Aleid, C. Zhang, W. Wang, P. Wang, *Cell Rep. Phys. Sci.* **2022**, 3, 100781.
[48] J. He, N. Li, S. Wang, S. Li, C. Wang, L. Yu, P. Murto, X. Xu, *J. Mater. Chem. A* **2022**, 10, 8556.
[49] Z. Li, T. Ma, F. Ji, H. Shan, Y. Dai, R. Wang, *ACS Energy Lett.* **2023**, 8, 1921.
[50] Z. Zhou, Y. Zhang, W. Liu, C. Gui, L. Huang, H. Huang, K. Fan, Y. Huang, Y. Gong, A. Chen, P. Liu, H. Jiang, *Desalination* **2024**, 583, 117685.
[51] H. Li, J. Ma, W. Yan, J. Lan, W. Hong, *Renewable Energy* **2024**, 235, 121277.
[52] Y. Li, C. Ni, R. Cao, Y. Jiang, L. Xia, H. Ren, Y. Chen, T. Xie, Q. Zhao, *Matter* **2024**, 7, 4270.
[53] J. Li, C. Xu, L. Chen, X. Zhang, M. Zhu, Y. Cheng, *Adv. Funct. Mater.* **2025**, 35, 2423063.
[54] H. Li, J. Liu, J. Kang, C. Dong, X. Niu, L. Zhang, Y. Li, X. Meng, W. Hong, *Small* **2025**, 21, 2408912.
[55] Y. Wang, S. Gao, H. Zhong, B. Zhang, M. Cui, M. Jiang, S. Wang, Z. Wang, *Cell Rep. Phys. Sci.* **2022**, 3, 100879.
[56] T. Li, M. Wu, J. Xu, R. Du, T. Yan, P. Wang, Z. Bai, R. Wang, S. Wang, *Nat. Commun.* **2022**, 13, 6771.
[57] S. Bai, Y. Tian, Y. Zeng, L. C. Chao, A. Pan, T. C. Ho, S. Chen, J. Shang, C. Y. Tso, *Appl. Therm. Eng.* **2023**, 225, 120163.
[58] W. Zhu, Y. Zhang, C. Zhang, X. Shan, A. K. Rao, S. L. Pitts, T. J. Woodbury, T. S. Masnyk, D. Derome, D. M. Warsinger, X. Ruan, L. J. Mauer, J. Carmeliet, T. Li, *Comms. Eng.* **2023**, 2, 35.
[59] J. Xu, X. Huo, T. Yan, P. Wang, Z. Bai, J. Chao, R. Yang, R. Wang, T. Li, *Energy Environ. Sci.* **2024**, 17, 4988.
[60] W. Zeng, H. Lin, Z. Sui, W. Wu, *Sci. Bull.* **2024**, 69, 2804.
[61] Y. Sun, Y. Ji, M. Javed, X. Li, Z. Fan, Y. Wang, Z. Cai, B. Xu, *Adv. Mater. Technol.* **2022**, 7, 2100803.
[62] R. H. Galib, Y. Tian, Y. Lei, S. Dang, X. Li, A. Yudhanto, G. Lubineau, Q. Gan, *Nat. Commun.* **2023**, 14, 6707.
[63] J. Zeng, X. Zhang, K. M. Chung, T. Feng, H. Zhang, R. S. Prasher, R. Chen, *Cell Rep. Phys. Sci.* **2023**, 4, 101250.
[64] L. Xu, D.-W. Sun, Y. Tian, L. Sun, Z. Zhu, *Chem. Eng. J.* **2024**, 479, 147795.
[65] X. Liu, P. Li, Y. Liu, C. Zhang, M. He, Z. Pei, J. Chen, K. Shi, F. Liu, W. Wang, W. Zhang, P. Jiang, X. Huang, *Adv. Mater.* **2024**, 36, 2409473.
[66] X. Hu, P. Hu, L. Liu, L. Zhao, S. Dou, W. Lv, Y. Long, J. Wang, Q. Li, *Matter* **2024**, 7, 4398.
[67] L. Yu, Y. Huang, Y. Zhao, Z. Rao, W. Li, Z. Chen, M. Chen, *ACS Appl. Mater.*

Interfaces **2024**, 16, 6513.
[68] Q. Ye, D. Chen, Z. Zhao, H. Yan, M. Chen, *Small* **2025**, 21, 2412221.
[69] L. Yu, Y. Huang, W. Li, C. Shi, B. W. Sheldon, Z. Chen, M. Chen, *Nano Res. Energy* **2024**, 3, e9120107.
[70] J. Shang, J. Zhang, Y. Zhang, X. Zhang, Q. An, *Nano Lett.* **2024**, 24, 7055.
[71] S. Zhuo, Z. Deng, Z. Wu, Y. Guo, Y. Wu, X. Zhao, Y. Han, B. Guo, *Prog. Polym. Sci.* **2024**, 155, 101856.
[72] J. Kim, G. Zhang, M. Shi, Z. Suo, *Science* **2021**, 374, 212.
[73] R. Zhu, D. Zhu, Z. Zheng, X. Wang, *Nat. Commun.* **2024**, 15, 1344.
[74] C. Cai, W. Chen, Z. Wei, C. Ding, B. Sun, C. Gerhard, Y. Fu, K. Zhang, *Nano Energy* **2023**, 114, 108625.
[75] M. Lian, W. Ding, S. Liu, Y. Wang, T. Zhu, Y.-E. Miao, C. Zhang, T. Liu, *Nanomicro Lett.* **2024**, 16, 131.
[76] R. Peeters, H. Vanderschaeghe, J. Rongé, J. A. Martens, *Environ. Sci.: Water Res. Technol.* **2020**, 6, 2016.
[77] H. Shan, P. Poredoš, Z. Chen, X. Yang, Z. Ye, Z. Hu, R. Wang, S. C. Tan, *Nat. Rev. Mater.* **2024**, 9, 699.
[78] X. Li, J. P. Gong, *Nat. Rev. Mater.* **2024**, 9, 380.
[79] J. Zeng, Q. Wang, Y. Shi, P. Liu, R. Chen, *Adv. Energy Mater.* **2019**, 9, 1900552.
[80] J. Xu, T. Li, T. Yan, S. Wu, M. Wu, J. Chao, X. Huo, P. Wang, R. Wang, *Energy Environ. Sci.* **2021**, 14, 5979.
[81] S. Wang, S. Li, N. Li, C. Wang, G. Cui, L. Yu, P. Murto, X. Xu, *Adv. Funct. Mater.* **2022**, 32, 2201919.
[82] D. Sun, K. F. Böhringer, *Microsyst Nanoeng.* **2020**, 6, 87.
[83] J. Yi, G. Zhang, H. Yu, H. Yan, *Nat. Rev. Mater.* **2024**, 9, 46.
[84] X. Wang, N. Wei, Y.-n. Chen, G. Ran, A. Zhang, H. Lu, Z. Wei, Y. Liu, W. Zhang, Z. Bo, *Natl. Sci. Rev.* **2024**, 11, nwae258.
[85] J. Wan, R. Zhang, Y. Li, Y. Li, *Wearable Electronics* **2024**, 1, 26.
[86] T. Liu, Y. Zheng, Y. Xu, X. Liu, C. Wang, L. Yu, M. Fahlman, X. Li, P. Murto, J. Chen, X. Xu, *Nano Energy* **2022**, 103, 107776.
[87] S. Huang, C. Qian, X. Liu, L. Zhang, F. Meng, Z. Yan, Y. Zhou, J. Du, B. Ding, J. Shi, A. Han, W. Zhao, J. Yu, X. Song, Z. Liu, W. Liu, *Sci. China Mater.* **2024**, 67, 2717.